DTRA-TR-99-39

Technical Report

High-Order Godunov Schemes for Multiphase Gas-Particulate Flowfield Modeling and Simulation

Approved for public release; distribution is unlimited.

September 2000

Prepared for:
Defense Threat Reduction Agency
45045 Aviation Drive
Dulles, VA 20166-7517

DSWA 01-97-C-0116

Jacob Krispin, et. al.

Prepared by: Krispin Technologies, Inc.
1370 Piccard Drive, Suite 210
Rockville, MD 20850

DESTRUCTION NOTICE:

Destroy this report when it is no longer needed. Do not return to sender.

PLEASE NOTIFY THE DEFENSE THREAT REDUCTION AGENCY, ATTN: ADM, 45045 AVIATION DRIVE, DULLES, VA 20166-7517, IF YOUR ADDRESS IS INCORRECT, IF YOU WISH IT DELETED FROM THE DISTRIBUTION LIST, OR IF THE ADDRESSEE IS NO LONGER EMPLOYED BY YOUR ORGANIZATION.

CUT HERE AND RETURN

DISTRIBUTION LIST UPDATE

This mailer is provided to enable DTRA to maintain current distribution lists for reports. (We would appreciate you providing the requested information.)

- ❑ Add the individual listed to your distribution list.
- ❑ Delete the cited organization/individual.
- ❑ Change of address.

Note:
Please return the mailing label from the document so that any additions, changes, corrections or deletions can be made easily. For distribution cancellation or more information call DTRA/ADM (703) 325-1036.

NAME: _____

ORGANIZATION: _____

OLD ADDRESS	NEW ADDRESS
_____	_____
_____	_____
_____	_____

TELEPHONE NUMBER: ( ) _____

DTRA PUBLICATION NUMBER/TITLE	CHANGES/DELETIONS/ADDITIONS, etc.) *(Attach Sheet if more Space is Required)*
_____	_____
_____	_____
_____	_____

DTRA or other GOVERNMENT CONTRACT NUMBER: _____

CERTIFICATION of NEED-TO-KNOW BY GOVERNMENT SPONSOR (if other than DTRA):

SPONSORING ORGANIZATION: _____

CONTRACTING OFFICER or REPRESENTATIVE: _____

SIGNATURE: _____

DEFENSE THREAT REDUCTION AGENCY
ATTN: ADM
45045 AVIATION DRIVE
DULLES, VA 20156-7517

DEFENSE THREAT REDUCTION AGENCY
ATTN: ADM
6801 TELEGRAPH ROAD
ALEXANDRIA, VA 22310-3398

REPORT DOCUMENTATION PAGE

Form Approved
OMB No. 0704-0188

1. AGENCY USE ONLY (*Leave blank*)	2. REPORT DATE	3. REPORT TYPE AND DATES COVERED
		Technical 970724-990731

4. TITLE AND SUBTITLE
High-Order Godunov Schemes for Multiphase Gas-Particulate Flowfield Modeling and Simulation

5. FUNDING NUMBERS
C - DSWA 01-97-C-0116
PE - RDT&E
PR - AC
TA - CE
WU - DH64698

6. AUTHOR(S)
Jacob Krispin, Mark Potts, Brady Brown, Ralph Ferguson and James Collins

7. PERFORMING ORGANIZATION NAME(S) AND ADDRESS(ES)
Krispin Technologies, Inc.
1370 Piccard Drive, Suite 210
Rockville, MD 20850

8. PERFORMING ORGANIZATION REPORT
KTI-TR-99-03

9. SPONSORING/MONITORING AGENCY NAME(S) AND ADDRESS(ES)
Defense Threat Reduction Agency
45045 Aviation Drive
Dulles, VA 20166-7517

CPWP/Frankel

10. SPONSORING/MONITORING AGENCY REPORT NUMBER
DTRA-TR-99-39

10. SUPPLEMENTARY NOTES
This work was sponsored by the Defense Threat Reduction Agency under RDT&E RMC code B 4662 D AC CE 5P01 A 25904D.

12a. DISTRIBUTION/AVAILABILITY STATEMENT
Approved for public release; distribution is unlimited.

12B. DISTRIBUTION CODE

13. ABSTRACT (Maximum 200 words)

The Computation All-Time Algorithm Package with Underlying Lawrence Technology (CATAPULT) is used to simulate the post-explosion evolution of cloud-rises resulting from the compromise of both confined and unconfined chemical and biological facilities. The evolution of nuclear clouds at relatively late (incompressible) times is also simulated. The results are compared with empirical and analytical data where available. In general, axisymmetric simulations do not accurately caption the physics of such flows in terms of cloud height, width, and rate of dissipation in comparison to three-dimensional simulations.

14. SUBJECT TERMS
Cloud Rise
Gas Dynamics
Compressible Flow
Dusty Gases
Incompressible Flow
Nuclear Cloud Rise
Projection Method

15. NUMBER OF PAGES
41

16. PRICE CODE

17. SECURITY CLASSIFICATION OF THIS PAGE	18. SECURITY CLASSIFICATION OF REPORT	19. SECURITY CLASSIFICATION OF ABSTRACT	20. LIMITATION OF ABSTRACT
UNCLASSIFIED	UNCLASSIFIED	UNCLASSIFIED	SAR

NSN 7540-01-280-5500

Standard Form 298 (Rev. 2-89)
Prescribed by ANSI Sta. 239-18, 298-102

Table of Contents

Figures

Figures (Continued)

Section 1
Introduction

This report describes the research and development work that was carried out between August 1, 1997 and August 1, 1999 under the DSWA SBIR Phase II Program in the area of High-Order Godunov (HOG) Schemes for Multiphase Gas-Particulate Flowfield Modeling and Simulation.

We describe here the development and extension of a major new capability for the HOG technology begun in our Phase I work and continued here. The new code developed here is based on both the Godunov scheme solution to the compressible Navier-Stokes equations and the projection method solution of the incompressible Navier-Stokes equations and provides high accuracy solutions to multi-phase flows ranging from high speed compressible flows to long time scale buoyant incompressible flows. This code has been used to simulate the two-phase plumes resulting from both confined and unconfined explosions of conventional warheads as well as to simulate the cloud rise phenomena associated with nuclear bursts in dry climates.

The Phase II objectives described in our proposal can be summarized as follows: to simulate gas-particulate cloud rise resulting from the compromise of both confined and unconfined CB facilities, to analyze the results and compare with experimental data and/or other models as available, and to modify, implement, and optimize algorithms, schemes, and codes in support of these simulations.

We have successfully met all of our objectives. A full simulation package, titled CATAPULT (Computational All-Time Algorithm Package with Underlying Lawrence Technology) has been developed to model multi-phase flows from explosion to fallout, spanning both compressible and incompressible fluid regimes. Simulations of explosions from both confined and unconfined CB facilities have been completed and the results analyzed and compared to existing data and models where applicable. Several modifications and optimizations have been included in the CATAPULT package to provide faster and more accurate solutions. In addition, simulations of nuclear cloud rise phenomenon have also been conducted using CATAPULT at the behest of the program director.

The sections below consist of a description of the governing equations, physical models and several extensions used here (Section 2), the numerical algorithms and extensions of our original codes by Krispin and Collins ([19] and Collins et al. [12]) are given in Section 3, and Section 4 describes the numerical results. The work is summarized in Section 5, including our main conclusions and several research and development issues that we find important and which we intend to pursue in future work. Included with this report is a compact disk containing the CATAPULT source code and instructions on compiling and running the model. Numerous results and animations of the work performed here may also be found on the included compact disk or at our website http://www.krispintech.com. This work also resulted in two publications, "Projection Methods for Incompressible Multiphase Cloud-Rise Phenomena" [8] and "Two Phase Plume Dynamics–a Comparison of Axisymmetric and Three Dimensional Simulations" [24]. The papers were both presented at the American Institute of Aeronautics and Astronautics summer meeting in Norfolk, VA and are included in electronic form on the enclosed CD.

Section 2
Governing Equations

2.1 Introduction.

The work accomplished during this program included modeling multi-phase flows in both the compressible and incompressible fluid regimes. The code used for the incompressible regime is based upon the work completed in Phase I [17] where underlying code technology used is the projection method for (single-fluid) incompressible flow that was introduced by Chorin [10] and updated in the late 1980's by Bell et al. [5] by using an unsplit high-order Godunov scheme to discretize the convection terms. In past work, Krispin and Collins [19] extended the projection method to two-phase, dusty-gas flows by incorporating ideas from Collins et al. [12] into the variable projection methodology of Bell and Marcus [6]. For this work, the methodology of Krispin and Collins [19] was used as the baseline code and it was developed and extended to the point that allows to simulate post-explosion, dusty-gas cloud rise dynamics. The compressible regime of the flow is solved using the technique of Collins et al. [12] and incorporates full adaptive mesh refinement (AMR) with gas and dust phases coupled in the same manner as in the incompressible code.

Reference [19] describes two numerical schemes for solving incompressible gas flows with embedded dust particles. The flow is modeled by extending the ideas described in Collins et al. [12] for the dusty-gas compressible fields to the incompressible gas limit. First, the Eulerian compressible conservation laws are used for the dust phase in the dusty-gas limit, where the dust particle pressure is zero and, as a consequence, all the eigenvalues are linearly degenerate and the fast modes are absent (see for example [11], [22]). For the gas phase, the incompressible Eulerian equations are used. The two phases are coupled via drag forces that are described as sources in the momentum equations of both phases. Also, gravity forces act on both phases. Following the work of [12], the limit of the resulting equations for a velocity equilibrium of both phases was analyzed in [19]; it was found that equilibrium solutions to this system exist only when the pressure gradient vanishes, resulting in a trivial solution. The above model is denoted the *non-equilibrium* model. A second and a relatively simple model for the dust phase that is incorporated in [19] is based on an a-priori assumption of velocity equilibrium among the two phases. The two-phase mixture is described by the incompressible equations and an additional equation models the advection of the dust density in the mixture velocity field, i.e., a tracer-like mechanism. This simple model is denoted the *equilibrium* model. The main conclusion of the work in [19] is that solutions obtained using the simplified equilibrium model are inherently different from solutions obtained using the non-equilibrium model described above: the solutions exhibit qualitatively different evolution patterns and quantitatively different dust density fields. This result lead us to focus on the further development of solvers to the non-equilibrium model only. This model is discussed in the following section.

2.2 Dusty Gas Model.

For the dust phase, the non-equilibrium dusty gas model of Miura and Glass [11] is used. This model assumes that the dust loading is sufficiently small such that the volume of the dust, or suspension phase, can be neglected, but the number of particles is large enough so that the suspension phase can be treated as a continuum. It is also assumed that the dust does not contribute to the pressure and is coupled to the gas phase only through the drag terms. Gravity forces are added to the momentum equations since these are important for many applications. The energy conservation equation for the dust phase is neglected since it fully decouples from the system in the absence of a gas energy equation (and hence heat transfer terms) and it does not contribute any desirable information for this model. The incompressible Euler equations for variable density, gas phase are as in [6] with the addition of the appropriate drag terms to the momentum equations. The system of equations for both phases based on these assumptions is:

$$\begin{aligned}
\mathbf{u}_t + (\mathbf{u}\cdot\nabla)\mathbf{u} &= \frac{\mathbf{1}}{\rho}\left(-\nabla\mathbf{p} + \rho\mathbf{g} - \frac{\sigma}{\mathbf{m}}\mathbf{D}\right), \\
\rho_t + (\mathbf{U}\cdot\nabla)\rho &= 0, \\
\nabla\cdot\mathbf{u} &= 0, \\
\sigma_t + \nabla\cdot(\sigma\mathbf{v}) &= 0, \\
(\sigma\mathbf{v})_t + \nabla\cdot(\sigma\mathbf{v}\mathbf{v}^{\mathbf{T}}) &= \sigma\mathbf{g} + \frac{\sigma}{\mathbf{m}}\mathbf{D},
\end{aligned} \tag{1}$$

where,

$$\begin{aligned}
\rho &= \text{gas density}, \\
\mathbf{u} &= \{u_i\} = \text{gas velocity vector}, \\
p &= \text{gas pressure}, \\
\sigma &= \text{dust density}, \\
\mathbf{v} &= \{v_i\} = \text{dust velocity vector}, \\
\mathbf{g} &= \text{gravity vector}, \\
\mathbf{D} &= D_i = \text{single particle drag vector}, \\
m &= \text{mass of a single dust particle}.
\end{aligned}$$

The particles are assumed to be spheres of diameter d. In past work we used the drag model as suggested in Miura and Glass [22]. That is,

$$\mathbf{D} = \frac{1}{8}\pi d^2\rho(\mathbf{u}-\mathbf{v}) \mid \mathbf{u}-\mathbf{v} \mid C_D, \tag{2}$$

where C_D is the drag coefficient given by

$$C_D = 0.48 + 28Re^{-0.85}. \tag{3}$$

$Re = \rho \mid \mathbf{u}-\mathbf{v} \mid d/\mu$ is the Reynolds number and μ is the gas viscosity.

2.3 Extensions to Physical Modeling.

The drag model given by Equations (2-3) is based on Stokes law and is not suitable for flows where the particles experience forces that accelerate them to ultra-Stokesian regimes. For example, setting dust particle diameter to 100 microns, the maximum Reynolds number in our sample flows ranges in order of magnitude from $\mathrm{Re}_{max} = O(10^2)$ (Gest experiments) to $\mathrm{Re}_{max} = O(10^3)$ (Priscilla calculations), which are 2–3 orders of magnitude (respectively) larger than the values for which Stokes law applies (Re= $O(1)$).

We have implemented, tested, and compared results for three additional drag models in this work. Equation (2) above is denoted Model 1 and the additional models chosen are:

(i) the model suggested by Godoy *et al.* [13] (denoted Model 2)

$$C_D = \begin{cases} \frac{24}{Re} & : \quad Re \leq 0.4207 \\ \frac{10^s}{Re} & : \quad Re > 0.4207 \end{cases}$$

where

$$s = \begin{cases} .133(\log_{10} Re) + 1.43 & : \quad 0.4207 < Re \leq 1.9368 \\ .116(\log_{10} Re)^2 + 0.0544 \log_{10} & : \quad Re + 1.443Re > 1.9368 \end{cases}$$

(ii) the model suggested by Wilson [26] (denoted Model 3) uses the drag coefficient given by

$$C_D = \begin{cases} \frac{24}{Re} & : \quad Re \leq 0.5 \\ \frac{24}{Re} + \frac{4}{Re^{\frac{1}{3}}} & : \quad Re > 0.5 \end{cases}$$

(iii) the model suggested by Chen and Pereira [9] (denoted Model 4) is given by,

$$\mathbf{D} = \frac{\alpha_p \rho_p}{\tau_p^*}(\mathbf{u} - \mathbf{v})\mathbf{f_p} \tag{4}$$

where α_p is the particle volume concentration, ρ_p is the mass density of the particle, i.e., $\sigma = \alpha_p \rho_p$; f_p is a correction factor (equivalent to coefficient of drag), depending on the particle Reynolds number; τ_p^* is the characteristic response time of the particle to the changes in fluid motion, given by $\tau_p^* = \frac{\rho_p d^2}{18\mu}$; and f_p is given by Boothroyd (see [9]) as follows:

$$f_p = \begin{cases} 1 + 0.15Re^{0.687} & : \quad 0 < Re \leq 200 \\ 0.914Re^{0.282} + 0.0135Re & : \quad 200 < Re \leq 2500 \\ 0.0167Re & : \quad Re > 2500 \end{cases}$$

Section 3
Numerical Method

3.1 General.

The solution of system (1) consists of coupling two distinctly different algorithms; the first three equations in system (1) describe the evolution of a variable density, gaseous phase of the flow field under the constraint of divergence free velocity field (i.e., incompressible flow). The solution of these equations follow closely the methodology described in [6], namely the projection method. The last two equations in (1) describe the conservation laws for the dusty, compressible phase of the flow field. These equations are solved using the ideas in [12]. The two algorithms are coupled to allow the appropriate modeling of the interaction (or coupling) terms of the equations, namely the drag forces $\mathbf{D} = \mathbf{D}(\mathbf{u}, \mathbf{v}, \rho)$. Some modifications of the cited algorithms were necessary in order to construct a consistent and complete methodology for the non-equilibrium model. In what follows we will discuss the main features of the underlying algorithms, starting with a brief description of the code of [19] and following with the necessary extensions applied in the current work.

3.2 The Modified Method of Krispin and Collins.

The basic methodology consists of first solving for an intermediate velocity field $\mathbf{u}^*$ and new density field using

$$\begin{aligned} \frac{\mathbf{u}^* - \mathbf{u}^n}{\Delta t} + [(\mathbf{u}\cdot\nabla)\mathbf{u}]^{n+1/2} &= \frac{1}{\rho^{n+1/2}}\left[\rho^{n+1/2}\mathbf{g} - \nabla p^{n-1/2} - \frac{1}{m}\frac{\sigma^n\mathbf{D}^n + \sigma^{n+1}\mathbf{D}^{n+1}}{2}\right] \\ \frac{\rho^{n+1} - \rho^n}{\Delta t} + [(\mathbf{u}\cdot\nabla)\rho]^{n+1/2} &= 0, \end{aligned} \tag{5}$$

where $\rho^{n+1/2}$ in Equation (5) is the average of ρ^n and ρ^{n+1}. A convection algorithm based upon a second-order unsplit Godunov scheme is applied to extrapolate velocities to cell faces at $t^{n+1/2}$. At this point in the algorithm, the normal velocities on cell faces are centered in time and second order accurate, but do not, in general satisfy the divergence constraint. In order to enforce the constraint before constructing the conservative updates, a MAC projection [3] is applied to the velocities at the intermediate time step $\mathbf{u}^{n+1/2}$ in order to obtain the face-based advection velocities $\mathbf{u}^{ADV}$. Continuing with the Godunov scheme, these advection velocities are then used to compute the conservative updates, namely $\rho^{n+1/2}$ and the velocity field $\mathbf{u}^*$ from Eq. (5) which does not, in general, satisfy the divergence constraint.

Then, a discrete projection $\mathbf{P}$ is applied to decompose the result of the first step into a gradient of a scalar potential and a divergence-free vector field. In particular,

$$\begin{aligned} \frac{\mathbf{u}^{n+1} - \mathbf{u}}{\Delta t} &= \mathbf{P}\left(\frac{\mathbf{u}^* - \mathbf{u}^n}{\Delta t} + \frac{\nabla p^{n-1/2}}{\rho^{n+1/2}}\right) \\ \frac{\nabla p^{n+1/2}}{\rho^{n+1/2}} &= (\mathbf{I} - \mathbf{P})\left(\mathbf{u}^* - \mathbf{u}^n\Delta t + \frac{\nabla p^{n-1/2}}{\rho^{n+1/2}}\right). \end{aligned} \tag{6}$$

Given some initial data at time level n the above algorithm requires an appropriate approximation for the velocity field of both phases, $\mathbf{u}$ and $\mathbf{v}$, and the densities of the gas and dust, ρ and σ, respectively, at time level n+1 for the calculation of the source term $\sigma^{n+1}\mathbf{D}^{n+1}$. An iterative procedure was constructed that, for each time step, starts with the initial guess for the $\nu = 0$ iterate, $\{\sigma, \rho, \mathbf{u}, \mathbf{v}\}^{n+1,\nu=0} = \{\sigma, \rho, \mathbf{u}, \mathbf{v}\}^{n}$ and repeats the computation of Equations (3) and (4) either until some convergence criteria is met or for a sufficient, fixed number of iterations ν. The update for the gas density, ρ^{n+1}, is given at the end of the calculation in Equation (3) whereas the update for the gas velocity, $\mathbf{u}^{n+1}$, is the end result of the projection step in Equation (4). The update for the velocity field of the dust phase, $\mathbf{v}^{n+1}$, together with the updated dust density, σ^{n+1}, are computed in an intermediate step which is embedded in the above iterative procedure. This step is based on the ideas in [12], as mentioned above, and it is discussed in [19] in great detail. The main limitation of the dust phase integration procedure is the fact that it is using the operator-split technique both for spatial and source integrations. This technique was modified as discussed in the following section.

3.3 Algorithmic Extensions.

We started this work by incorporating Colella's unsplit methodology [11] in the dust phase of our original code [19]. As a consequence, source integration in the dust phase can be performed in an unsplit fashion which is a necessary requirement for stable and accurate integration of stiff source terms (see, e.g., conclusions of the studies in [18] and [20]).

The new conservative-difference corrector step of the dust phase, written in two-space dimensions, is given by,

$$\begin{aligned}\mathbf{W}_{j,k}^{n+1} &= \mathbf{W}_{j,k}^{n} - \alpha_x \left[\mathbf{F}_{j+1/2,k}^{n+1/2} - \mathbf{F}_{j-1/2,k}^{n+1/2}\right] - \\ &\quad \alpha_y \left[\mathbf{G}_{j,k+1/2}^{n+1/2} - \mathbf{G}j, k - 1/2^{n+1/2}\right] + L\mathbf{S}(\mathbf{W}_{j,k}^{n+1}, \mathbf{W}_{j,k}^{n}) \qquad (7)\end{aligned}$$

where $\mathbf{W}$, $\mathbf{F}$, $\mathbf{G}$, and $\mathbf{S}$ are defined in the obvious way (using Equation(1)), $\alpha_x = \frac{\Delta t}{\Delta x}$, $\alpha_y = \frac{\Delta t}{\Delta y}$, and L denotes a source-term integration operator. We tested two operators, given by

$$L_1 = \frac{\Delta t}{2}(\mathbf{S}(\mathbf{W}_{j,k}^{n+1}) + \mathbf{S}(\mathbf{W}_{j,k}^{n})) \qquad (8)$$

and

$$L_2 = \Delta t \mathbf{S}(\mathbf{W}_{j,k}^{n+1}). \qquad (9)$$

Other algorithmic extensions involve cycling and subcycling needed to iterate on the implicit (or semi-implicit) variables that are coupled between the two phases, in particular the velocity fields. Several user-defined iteration counts are built into the code and they are problem dependent.

Section 4
Numerical Results

4.1 Convergence Study.

The rate of convergence for the method discussed above is investigated for a smooth initial stream function and density field inside a unit square defined exactly as in [6],

$$\Psi(x,y) = \pi^{-1} sin^2(\pi y) sin^2(\pi x), \rho(y) = 1 - \frac{1}{2} tanh(y - \frac{1}{2}). \tag{10}$$

The initial velocities are defined in the usual way by $u = \partial\psi/\partial y$ and $v = -\partial\psi/\partial x$. The initial dust density $\sigma = 0.01\rho$, and the initial dust velocity $\mathbf{v} = \mathbf{u}$. The velocities for both phases satisfy homogeneous Dirichlet boundary conditions and the density for both phases is determined through a second-order extrapolation from the outermost interior cells. The gravity term was removed for the purposes of this study. The solution is computed on uniform grids $\Delta x = \Delta y = 1/2^n$ for 2^n uniform time steps at a CFL = 0.5 for n = 4, 5, 6, 7. The second normal residual is measured between grids of adjacent resolution and is used to calculate the rate of convergence which are summarized in Table 1. The gas density and velocity fields for the coupled system retains a second-ordered accuracy with a slight deterioration similar to that reported in [6] for the single-phase system. The convergence rate for the particle density and velocity fields indicate an accuracy between first and second order. This is due to the difficulties of accurately-predicting the flux terms in the particle-phase, particularly in regions where vacuum states or colliding particle streams occur. Such limitations of the particle-phase model are also discussed in [12] for compressible flows. Modifications to reduce the limitations of the particle-phase model are currently under investigation

Table 1. Rates of convergence.

Variable	32-64	Rate	64-128	Rate	128-256
ρ	5.612e-04	2.12	1.245e-04	1.94	2.217e-05
$\mathbf{u}$	3.025e-03	1.87	8.628e-04	1.77	2.746e-04
σ	5.908e-04	1.34	3.271e-04	1.34	1.810e-04
$\mathbf{v}$	5.589e-03	1.42	2.791e-03	1.37	1.477e-03

4.2 Validation.

In the same manner as that of Krispin and Collins [19], the numerical scheme with the algorithmic extensions described in section 3.3 is initially tested by simulating low density bubbles containing a dust phase. The gas density of an initially spherical bubble is specified to be one tenth the density of the surrounding ambient gas. The density of the dust particle phase is specified to be one hundredth of the density of the bubble's gas phase. The bubble is initially at rest.

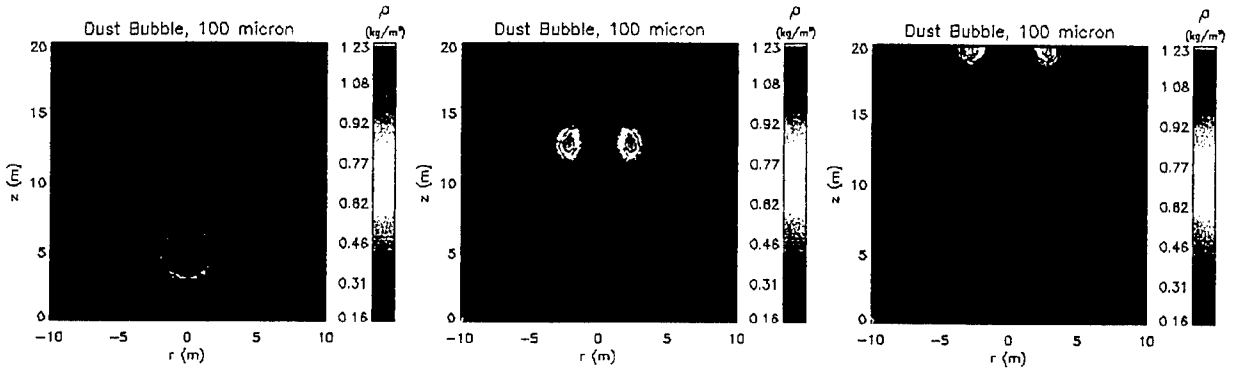

(a) 0 seconds (b) 2.5 seconds (c) 5.0 seconds

Figure 1. Gas and dust density contours for simulation of a dusty bubble with 100 micron dust particles.

Figure 1 shows the result for an axisymmetric calculation for a dusty bubble with a 100 micron particle-phase. The simulation is from time zero to 5.0 seconds. The color scale depicts the density of the gas-phase, where blue indicates lower densities and red higher densities. Ten contour lines map out the log10 density of the dust-phase. The velocity vectors depict the gas-phase velocities.

Gravity is oriented in the usual direction. As the low density gas bubble rises, the dust near the top of the bubble rises as well, entrained in the resulting gas velocity field. The dust in the region around the lower portion of the bubble falls due to the gravity field. As expected rate of fallout at of the dust in the lower portion of the bubble is found to be sensitive to the specified particle diameter. The test case in Figure 1 has a grid resolution of 32x64 for a physical domain of 10x20 meters.

Figure 2 shows a three-dimensional dusty bubble simulation where in this case, the particle-phase is modeled as an advected scalar in the same manner as the AD scheme described in Krispin and Collins [19] (although here we now utilize the projection method described in section 3.3). The lefthand frame depicts a blue gas density isosurfaces and black log particle density isosurfaces. The righthand frame shows a slice of the flow field in the x-z plane at approximately y = 10 meters. Similar to the two-dimensional simulations, the color scale depicts the gas density, the black line contours map the log of the dust density, and the velocity vectors indicate the motion of the gas phase. The gas density in the bubble is less than that of the surrounding ambient gas. This causes the bubble to rise while continuously entraining the heavier ambient gas.

In the same manner as the two-dimensional axisymmetric cases, the simulation is from time zero to 5.0 seconds. The dust density for infinitely small particles is computed through a single advection equation, i.e., the dust particles are completely entrained into the gas-phase flow and are simply advected with the gas.

This test case has a coarse grid of 32x32x32 cells for a domain of 20 meters cubed. A runtime of approximately 0.5 CPU hours on a 400 MHz Pentium II processor is required to advance the solution to 5.0 seconds.

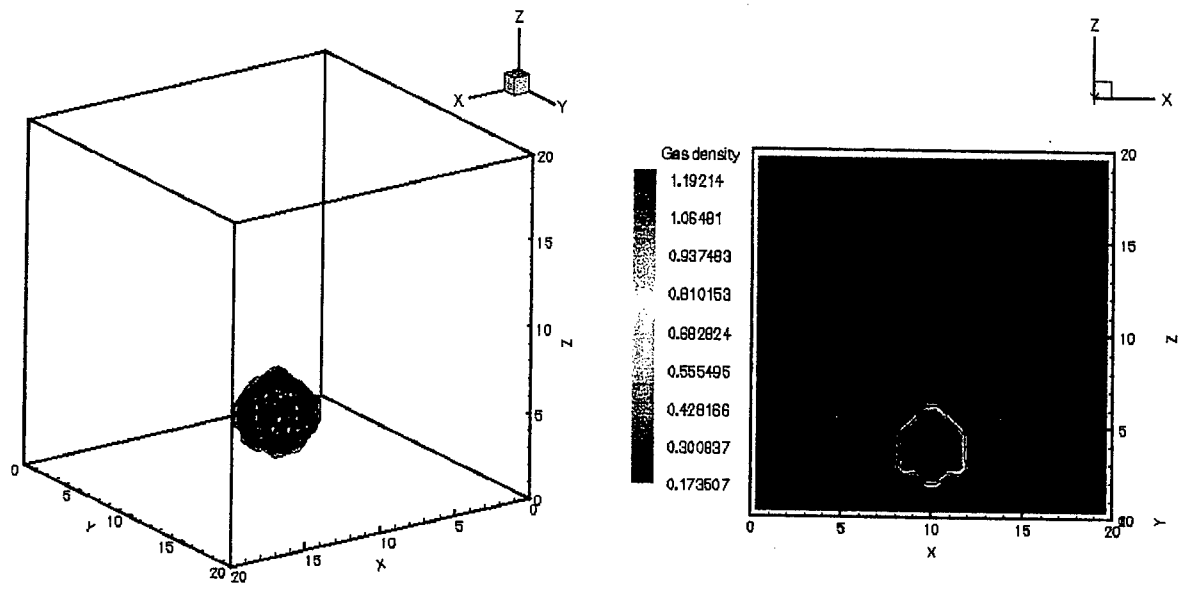

(a) 0 seconds

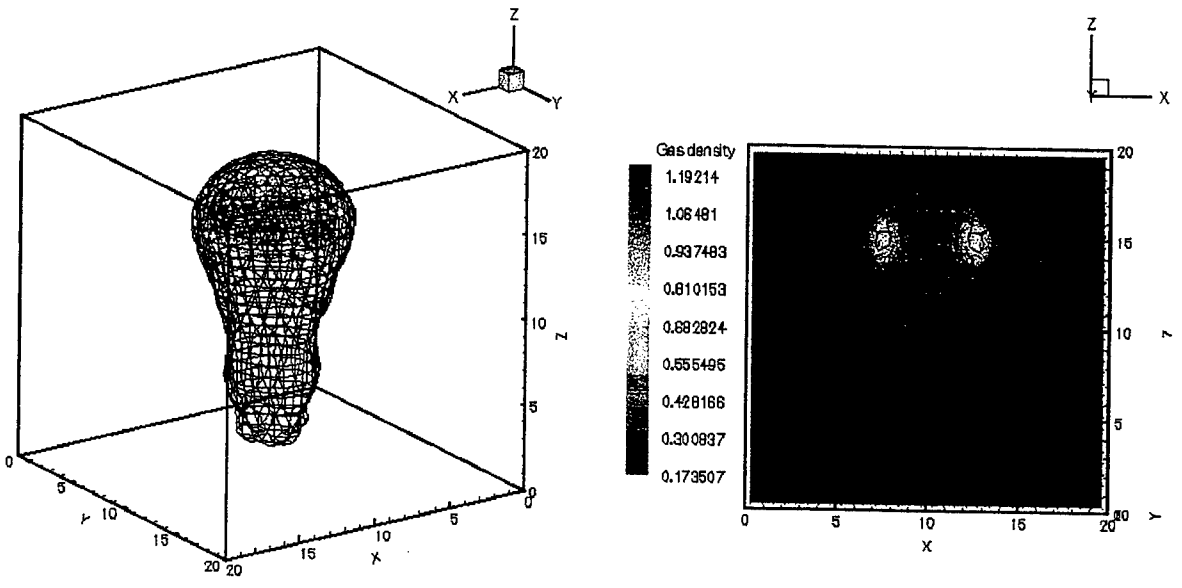

(b) 3.0 seconds

Figure 2. 3-D isosurfaces of gas density (blue) and Log(dust density) (black) on the left and gas and dust density contours from an x-z cross section on the right.

In summary, both the multi-phase model and single phase advection model result in the same qualitative trends for rising dusty bubbles as those described in Krispin and Collins [19] for both axisymmetric and three-dimensional simulations.

4.3 Confined Explosions.

For a number of reasons including the availability of model input data and experimental results, the bulk of our effort was spent on the simulation of confined explosions. The problem however, involves both compressible and incompressible flow regimes, so the simulation was undertaken in sections. Initially, the compressible portion of the simulation was accomplished by simply using the plume size and mass distribution prediction by Applied Research Associates' (ARA) STructural Expulsion and Plume (STEP 2.3) model. [14] Using STEP data as a starting condition for the incompressible model proved to be a poor choice for for initial conditions however. The plume predicted by STEP as early as 8.4 seconds was negatively buoyant and fell quickly to earth after mapping to CATAPULT. Figure 3 shows the evolution of the plume when mapped from STEP input from 8.4 seconds. One of the primary reasons for this collapse is most likely due to the lack of a stratified atmosphere in the STEP code which models the atmosphere as an infinite room with a constant air density. STEP is also based on empirical data and linearized equations which result in inaccurate predictions of dust and gas distribution inside the plume.

After determining that STEP provided a poor density distribution for the input to the incompressible model, it was decided that a realistic simulation of the plume required modeling the compressible phase of the problem as well as the later incompressible stages. The compressible phase of the plume was modeled using vent data that was also provided by STEP. However, since it is more difficult to predict realistic 3-D velocity and density *distributions* than it is to predict velocity and density at a *point* (the vent), it was assumed that the vent data would be more accurate than the distribution predictions used earlier.

The results from the DIPOLE EAST experiment in New Mexico indicated that the plume should rise to approximately 120 meters in height after 10 seconds, while spreading to a width of approximately 35 meters in the same time. The results then show that the plume rises to a height of approximately 325 meters and an average width of 180 meters over the following couple of minutes before dissipating. STEP predictions, which are based primarily upon empirical data fits from similar experiments also predict that the plume initially rises quickly (0-10 seconds) to a level of approximately 150 meters and spreads to a diameter of 20 meters over the same time. These results correspond to spreading rates (dr/dz) for the plume of 0.146 and 0.073 for the experiment and STEP respectively over the first ten seconds of the flow.

4.3.1 Compressible Phase.

Initially, an axisymmetric compressible model was used to simulate the compressible portion of the experiment, but problems were soon discovered with that approach. Using both Logicon R&D Associates report on the DIPOLE EAST 159 experiment[2] and plume height predictions from

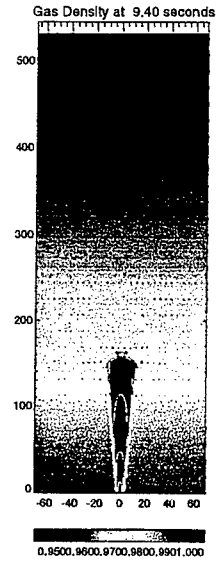

(a) Time = 9.4 seconds

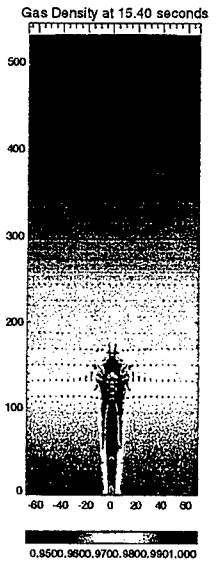

(b) Time = 15.4 seconds

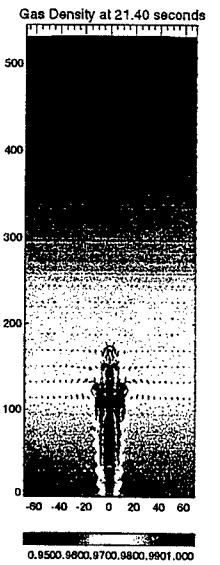

(c) Time = 21.4 seconds

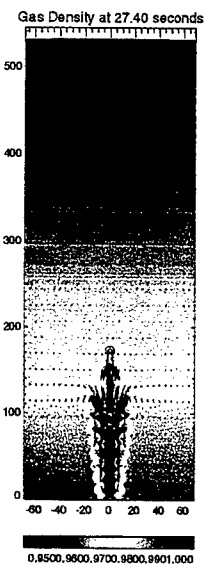

(d) Time = 27.4 seconds

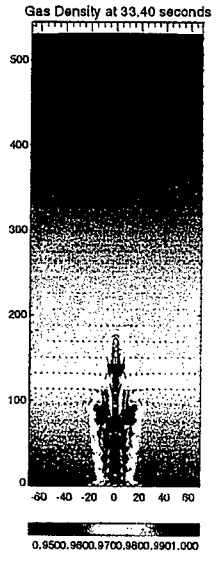

(e) Time = 33.4 seconds

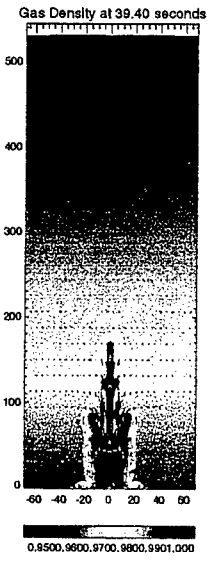

(f) Time = 39.4 seconds

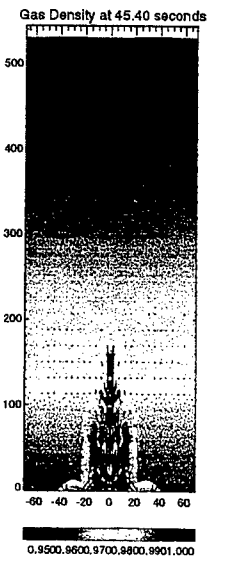

(g) Time = 45.4 seconds

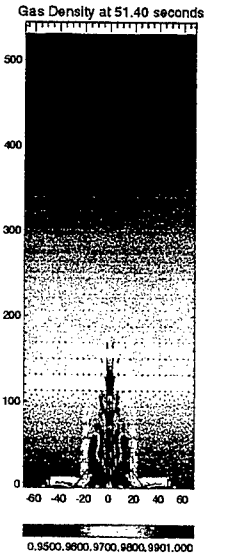

(h) Time = 51.4 seconds

Figure 3. Gas density color contours with Log(dust density) contours overlain for incompressible run initialized with STEP data.

STEP as a basis, it quickly became apparent that the axisymmetric model was predicting plume heights that were entirely too high.

Several axisymmetric runs using full AMR were undertaken and one was conducted out to more than two seconds. In every axisymmetric case, the plume spreading rate was extremely small and the plume height predictions were advancing too rapidly. Perturbations were introduced to both the ambient atmosphere and radial velocity but did not significantly affect this outcome. Despite the efforts to induce instability in the flow and enhance plume spreading and slowing, all axisymmetric compressible runs resulted in unrealistically high and narrow plumes.

Figure 4 shows the plume heights predicted by axisymmetric, and three dimensional simulations as well as the baseline prediction by STEP. The curves clearly show that axisymmetric simulations even when performed at high resolution with AMR are not able to capture the physics of the problem, whereas the three dimensional simulation is better able to do so even when run on relatively coarse resolution grids. The axisymmetric runs displayed a large variety of vortex rings and roll-ups along an otherwise very narrow jet-like structure. The vortex formations along the jet flow can be seen in Figure 5 which shows gas density for the entire plume at several times in one simulation as well as a closer view of the base of the plume at 0.326 seconds. Clearly evident in the figure, the plume exhibits little spreading and the plume height is considerably higher than that seen in either experimental results or STEP predictions shown in Figure 4. The fourth panel in Figure 5 exhibits the considerable turbulence that is evident along the centerline of the domain and is found at all heights along the jet. Despite this turbulent energy sink, the plume did not slow or spread appreciably, indicating that the main mode for energy transfer occurs elsewhere in the problem.

Analysis of the plume spreading rate in the early times of the axisymmetric simulations shows that it is between 0.1 and 0.3 (depending on where the edge of the plume is determined to be) which is right in line with the spreading rates in the near field reported by Kouros et al.[16] and the experimental results. The plume tip is also only at 35 meters or 58 d_0 downstream at this point. The problem arises at later times when the plume has not continued to spread away from the axis. At approximately a second after the blast, the plume has continued to rise with little or no spreading, reducing the spreading rate to 0.032. The tip of the plume at this point is at nearly 200 meters or 316 d_0 downstream. Experimental jets and plumes[21, 16] generally show that axisymmetry begins to break between 50 and 100 d_0 and a three dimensional simulation is required to capture the correct asymmetric motions.

Since attempts to induce instability in the axisymmetric simulations by introducing density and inflow velocity perturbations were unsuccessful, it became apparent that the axisymmetric formulation itself was not capturing the full physics in the problem and full three dimensional simulations were undertaken. The 3D simulation was run to a time of 10 seconds before being mapped to an incompressible grid. A series of plots show gas and dust density isosurfaces for 10 times throughout the 3-D simulation in Figure 6. The axisymmetry in the problem is already beginning to break in the first frame at a time of 0.73 seconds and the flow is definitely asymmetric by frame 2 which is at a time of 1.4 seconds. This trend toward asymmetry is observed in both the dust and gas isosurfaces throughout the simulation as the plume height reaches more than 120 meters by a time of 8.1 seconds, matching STEP and DIPOLE East results

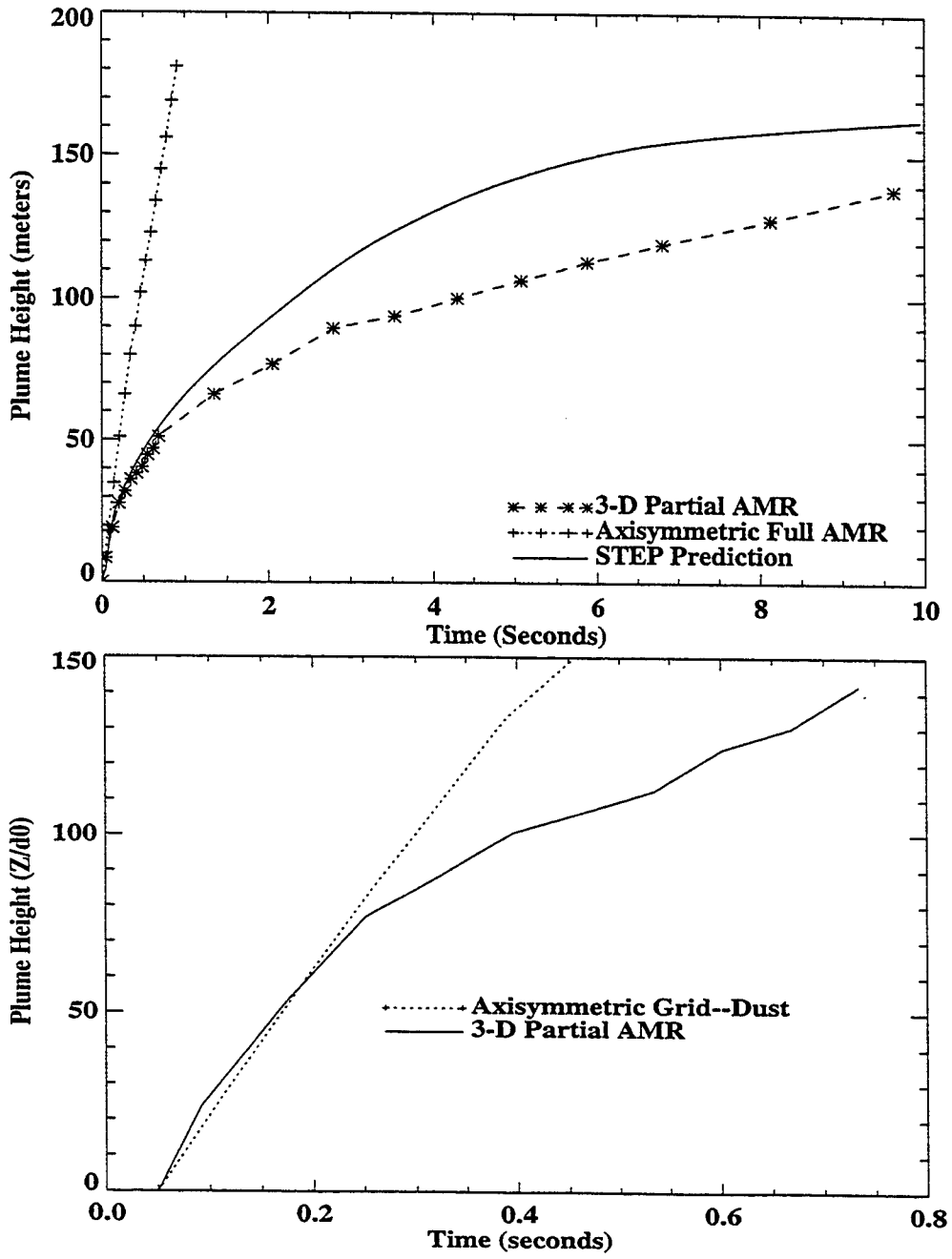

Figure 4. Plume heights from axisymmetric, 3D, and STEP simulations (above) and a blow up view of axisymmetric and 3D simulations at early times (below).

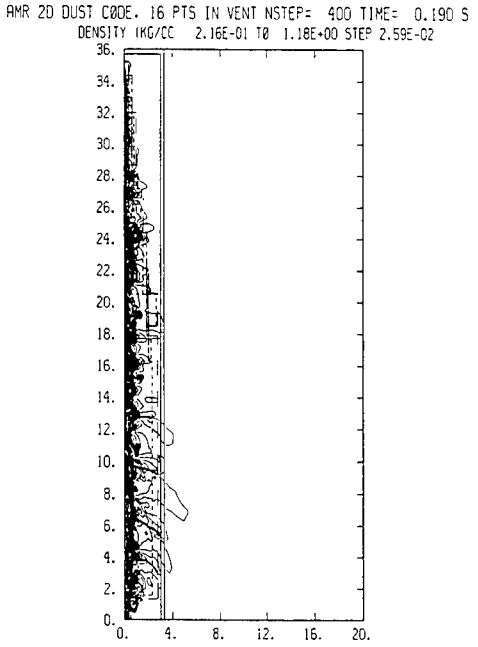

(a) Plume density at time 0.190 seconds.

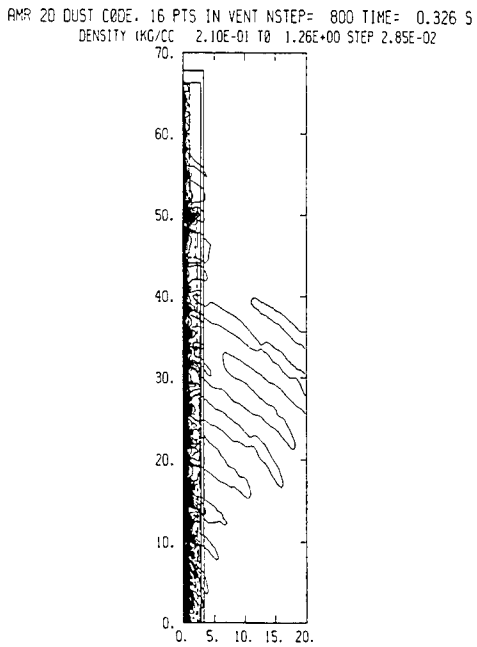

(b) Plume density at time 0.326 seconds.

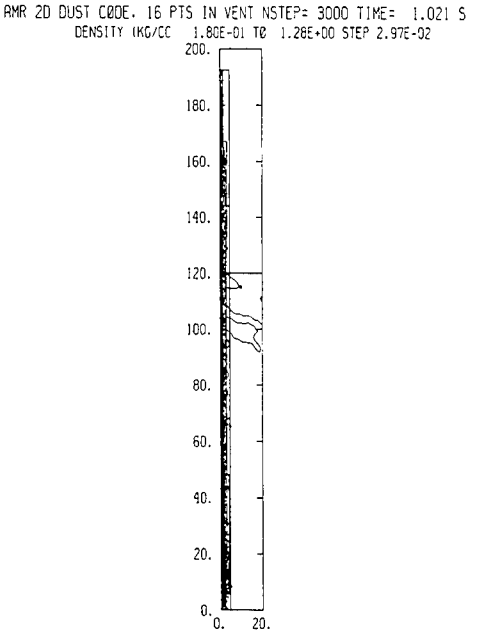

(c) Plume density at time 1.021 seconds.

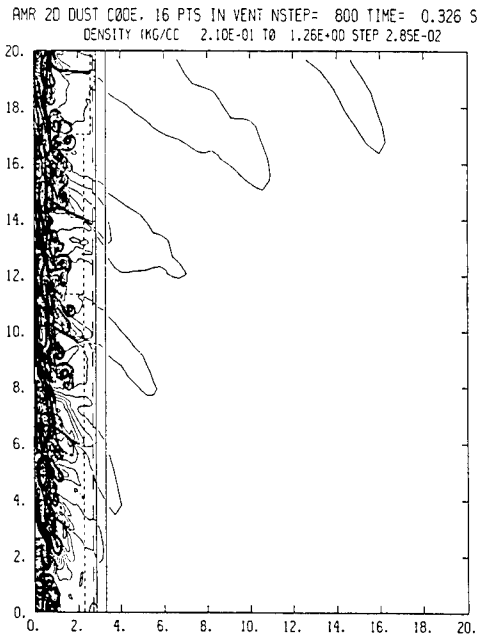

(d) Plume density from 0 to 20 meters at 0.326 seconds.

Figure 5. Plume gas density at various times from axisymmetric simulations.

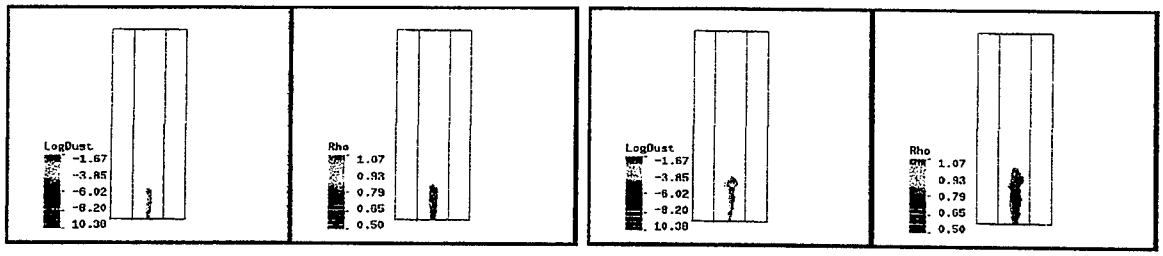

(a) Time = 0.73 seconds

(b) Time = 1.4 seconds

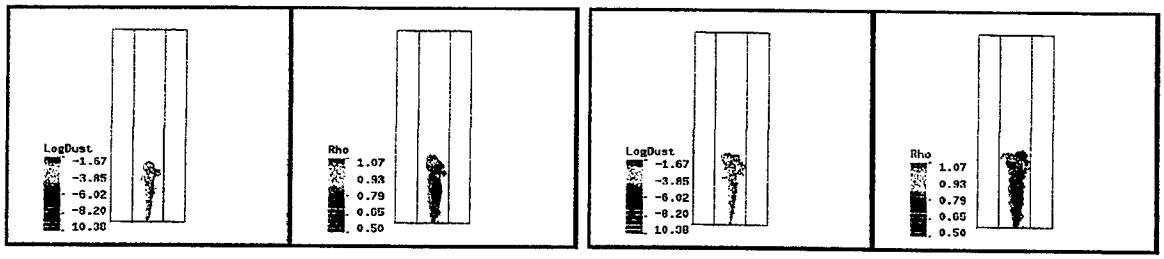

(c) Time = 2.1 seconds

(d) Time = 2.8 seconds

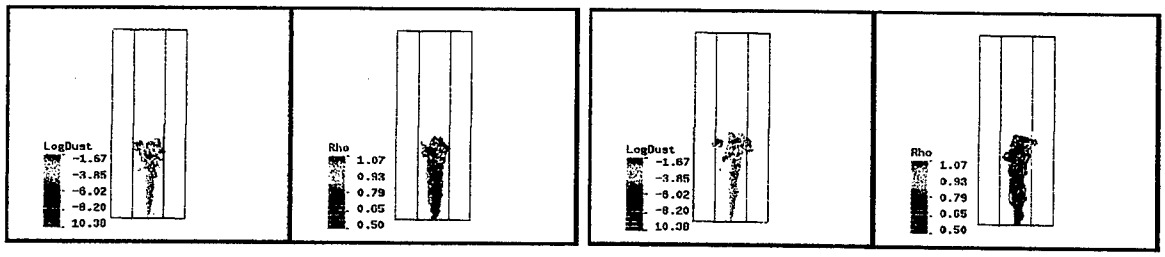

(e) Time = 3.6 seconds

(f) Time = 4.4 seconds

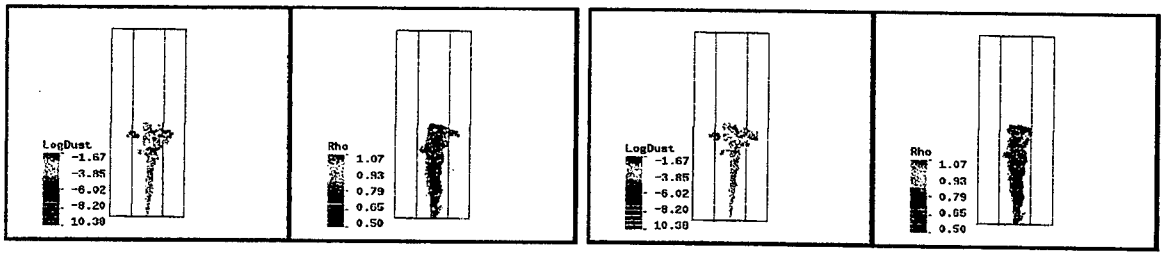

(g) Time = 5.1 seconds

(h) Time = 5.9 seconds

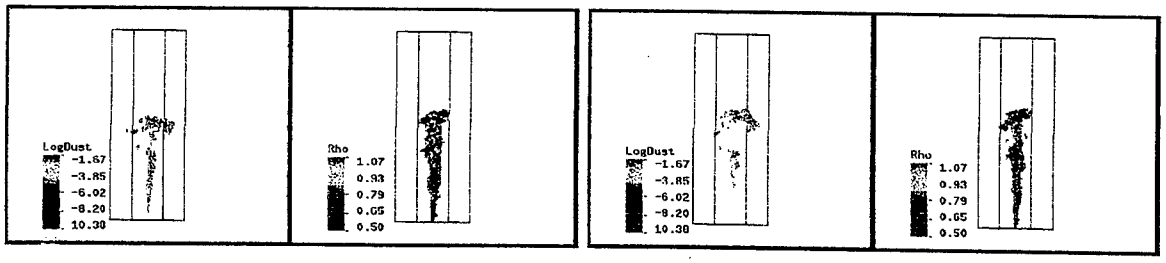

(i) Time = 6.9 seconds

(j) Time = 8.1 seconds

Figure 6. Gas density isosurface (left panels) colored according to the Log of dust density and dust density isosurface (right panels) colored according to gas density.

quite well. Three dimensional results began diverging noticeably from axisymmetry at around half a second after the blast, and this divergence significantly affected the plume height and spreading rate. As is evident in Figure 4, both axisymmetric and 3D simulations agree very closely for the first 0.33 seconds of the flow. The spreading rate for both simulations are likewise similar up to this time. At around 0.33 seconds however, the tip of plume in the 3D simulation begins to expand and move off the centerline of the domain which appears to be the primary cause of the slowing in the 3D simulation and in real plumes. It should be noted that the divergence does not occur until the tip of the plume has achieved a height of nearly $100d_0$, which is as much as most jet flow simulations and experiments in the literature capture of the flow at all.

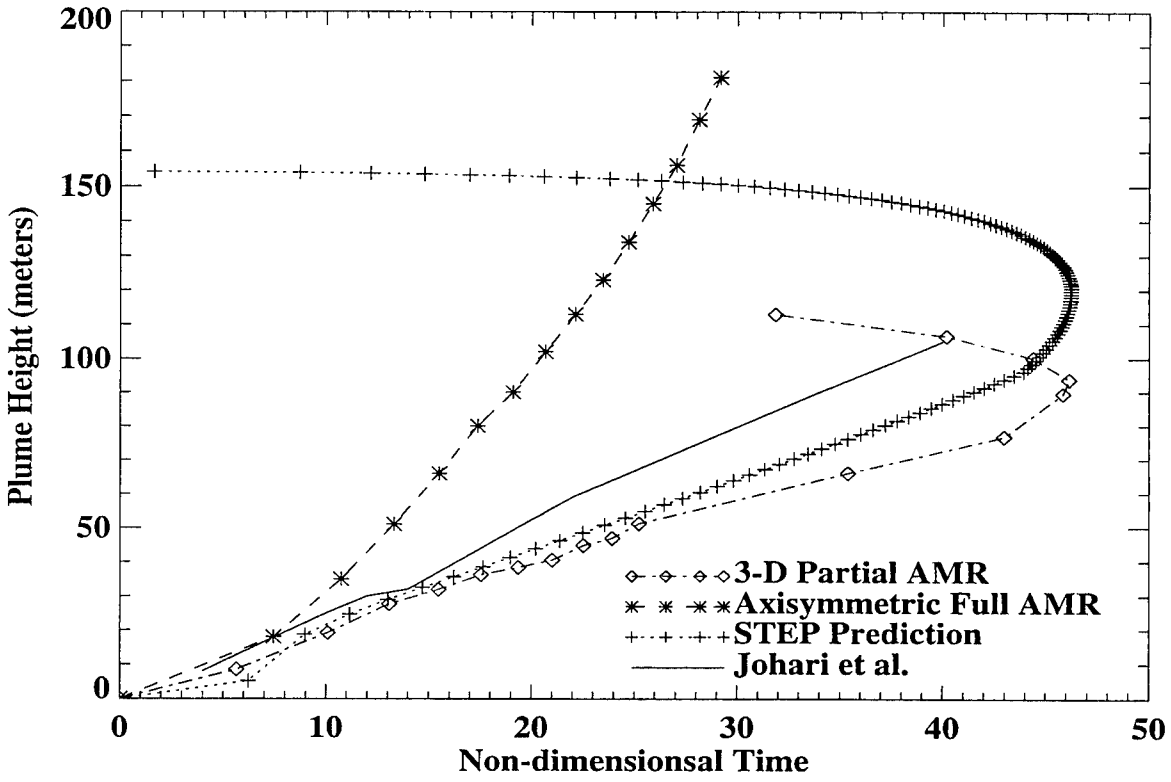

Figure 7. Plume heights vs. square root of non-dimensional time $(V_j t d^{-1})^{0.5}$.

Johari et al. [15] have shown that impulsively started jets display a starting vortex that scales in a self similar manner as the square root of non-dimensional time $(tV_j d_0^{-1})$. A plot of the data shown in Figure 7 from both axisymmetric and fully 3D simulations shows that all initially display a linear trend similar to that seen by Johari et al. The slope of the axisymmetric simulations diverges quickly from the STEP prediction and the 3D simulation, but all three display a mostly linear trend through the majority of the simulation. As the vent inflow velocity drops rapidly to zero a reversal of non-dimensional time occurs and is responsible for the switch-backs seen in the STEP and 3D curves. Both the STEP and 3D curves fall slightly below the results reported by Johari et al. (also shown on the figure), while the axisymmetric run falls above all the others by a considerable margin. The slope reported by Johari et al. is approximately 2.7 whereas the 3D simulation predicts a slope of roughly 1.95. The differences in slopes may indicate that plume

penetration slows at higher Reynolds numbers or that compressible effects and gravity are slowing the plume.

Typical averaged velocity profiles for a steady state turbulent jet follow a self-similar solution that has been fairly well established. [25] When scaled by the axial velocity (W/W_{ax}) and plotted against axial distance over radial distance (Z/R), the velocity profile collapses to $sech^2(Z/R)$. Atassi et al. [4] have shown that transient jets can be expected to follow a modified self-similarity as well. It has been shown that when far enough removed from the jet source, the velocity profile of an unsteady jet is the same as that seen in a steady jet. [16] The assumption however, is that the jet oscillates around some non-zero average, which is somewhat different than the case presented here.

Since the velocity profile is scaled by the velocity along the axis, it is not unreasonable to expect an unsteady decaying plume to behave similarly. Figure 8 shows the self-similar velocity structure from the 3D compressible simulation of the plume over several different time steps. There is a significant amount of scatter in the data, but the velocity generally follows the expected velocity profile which is plotted as a solid line. Initially, the profiles from higher altitudes, which are plotted as stars, are scattered fairly evenly above and below the theoretical profile, but at later times, they fall consistently below the theoretical curve, especially at larger values of R/Z. This is most likely indicative of gravity beginning to effect the flow. The tightening of the profile at higher altitudes also lends credence to the idea that instability increases away from the axis of symmetry. The general conformance to the self-similar profiles for steady jets indicates that the overall flow still conforms to an ensemble axial symmetry. However, the comparisons of 3D and axisymmetric simulations with empirical models and experimental results show undeniably that the strict enforcement of axial symmetry produces incorrect values for both plume height and spreading rate. This leads us to the conclusion that compressible axisymmetric simulations are inadequate in capturing the real physics in jet and plume problems. While results may be fairly accurate in the near field, by the time the flow has reached 50 d_0, the axial symmetry is no longer appropriate.

Volume entrainment in a plume or jet can be computed as the volume of gas that is within the plume flow field. This reduces to a summation of gas density multiplied by vertical velocity and grid cross sectional area given as

$$Q = \sum_{i=1}^{nx} \sum_{j=1}^{ny} \rho_{ij} w_{ij} dx dy \tag{11}$$

and is computed at every z level in the flow. This yields a volume flow rate at each level in the z direction at any given time. Bremhorst and Hollis [7] have shown that the entrainment rate for a fully pulsed jet is nearly twice that observed in steady jets in the near field. They also found that the volume entrainment rate scaled as a nearly linear function of x/d. Figure 9 is a contour plot of volume entrainment as a function of time and distance. The volume entrainment during the compressible phase of the 3D plume simulation is roughly linear at lower values of z/d as noted by the regular spacing in contour levels up to a level of $z/d \approx 75$. The entrainment curve exhibits a strongly increasing trend at higher levels of z/d before dropping precipitously at the top of the plume. The entrainment rate is also a function of time as well. As time progresses, the entrainment increases in volume as the main area of entrainment propagates away from the vent. The near field volume entrainment rate is higher than that reported for steady jets at early times, but less than the rate reported by Bremhorst and Hollis, falling at approximately 1.5 times the

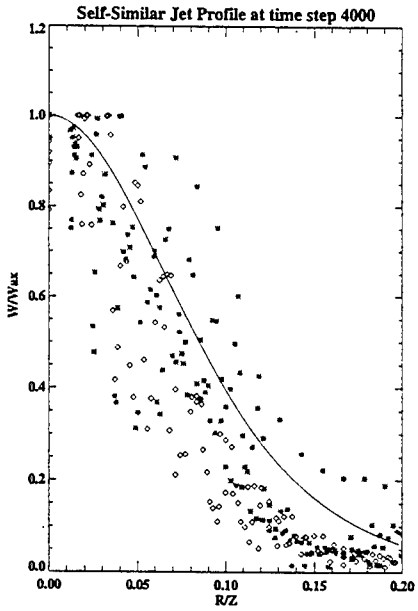

(a) Self-similar velocity profile at 2.84 seconds.

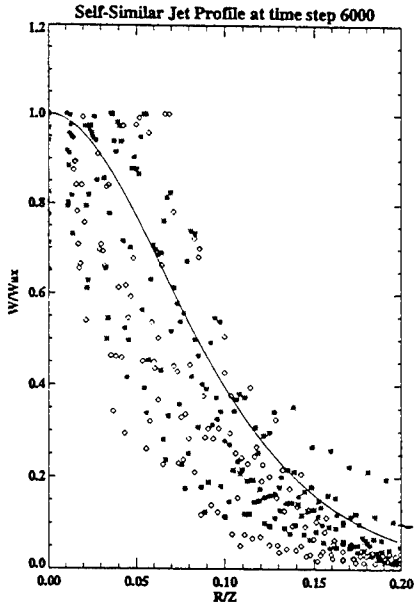

(b) Self-similar velocity profile at 4.35 seconds.

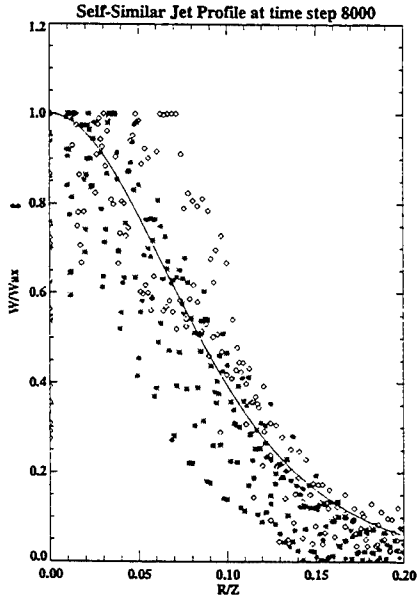

(c) Self-similar velocity profile at 5.93 seconds.

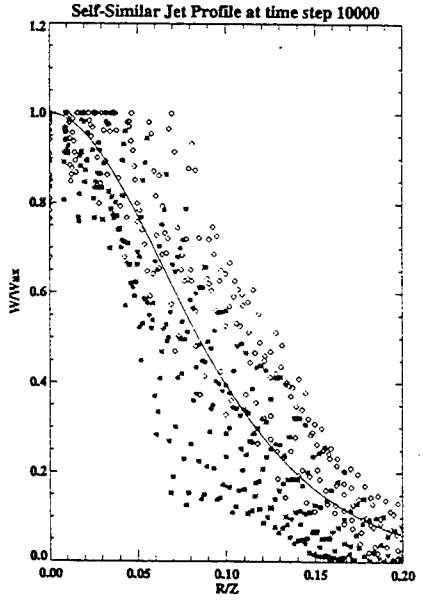

(d) Self-similar velocity profile at 8.18 seconds.

Figure 8. Self-similar plume velocity profiles from various times. Stars indicate velocities from higher altitudes while diamonds represent lower altitudes in the plume. The line is the theoretical jet velocity profile.

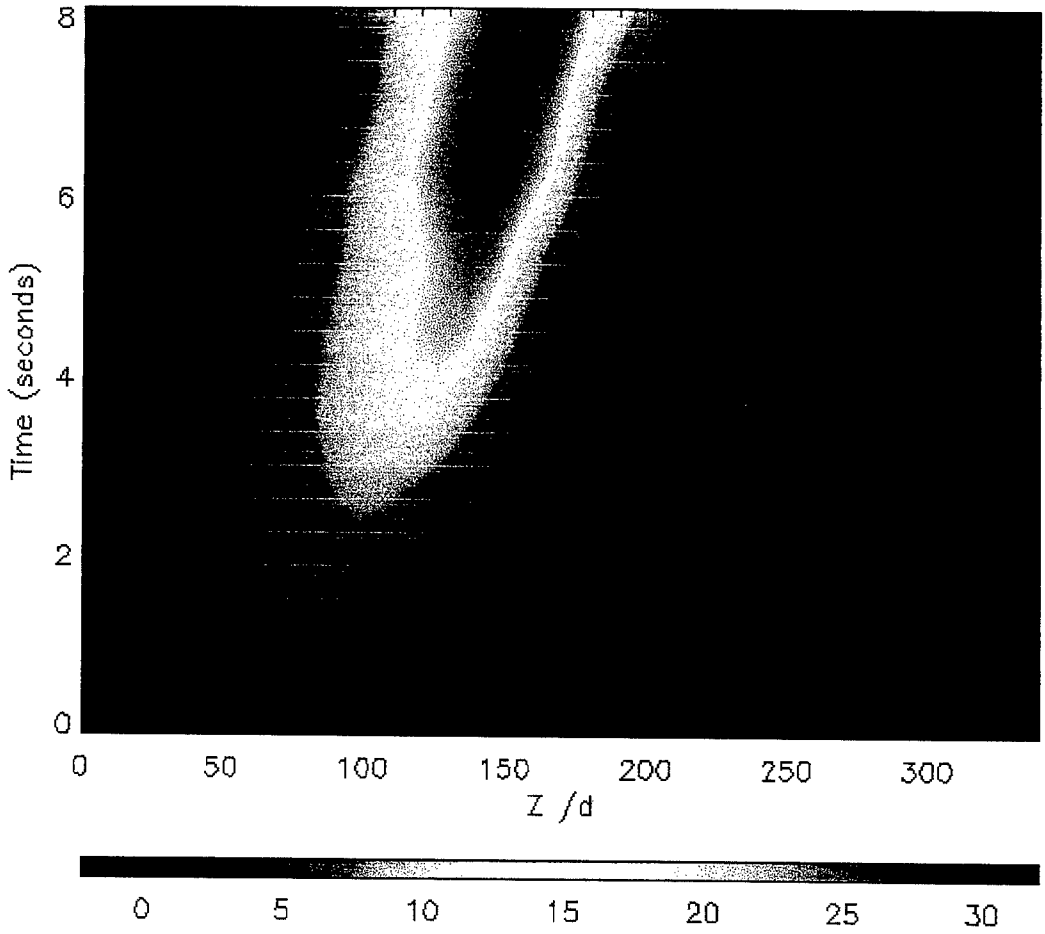

Figure 9. Contour plot of normalized entrainment rate (Q/Q_E) as a function of Z/d_0 and time.

steady rate. As the entrainment area propagates away from the vent however, the rate of entrainment increases non-linearly to a maximum value of 114 Q/Q_E at 154.7 Z/d_0, where Q/Q_E is the volume flow rate normalized by the inflow rate. Although Bremhorst and Hollis did not report volume rates at these distances, if their reported entrainment rate continues in a linear fashion, it would be approximately 117 Q/Q_E at 154.7 x/d_0. The increasing entrainment rate in the far field may suggest that the optimal mixing region in conventional jets occurs at distances beyond those investigated in previous experiments.

Longmire and Eaton[21] have shown that for two-phase flows, particles congregate in areas of gas divergence while they are likely to be sparse in areas of convergence. The largest areas of divergence in this flow also have a tendency to show higher concentrations of dust. Figure 10 shows an Y-Z cross section of the plume at times of 5.1 and 6.9 seconds with the shaded contours showing gas divergence and the line contours, dust density. The correlation is not exact, but higher dust densities are generally in the darker or divergent regions of the plot just as predicted by Longmire and Eaton.

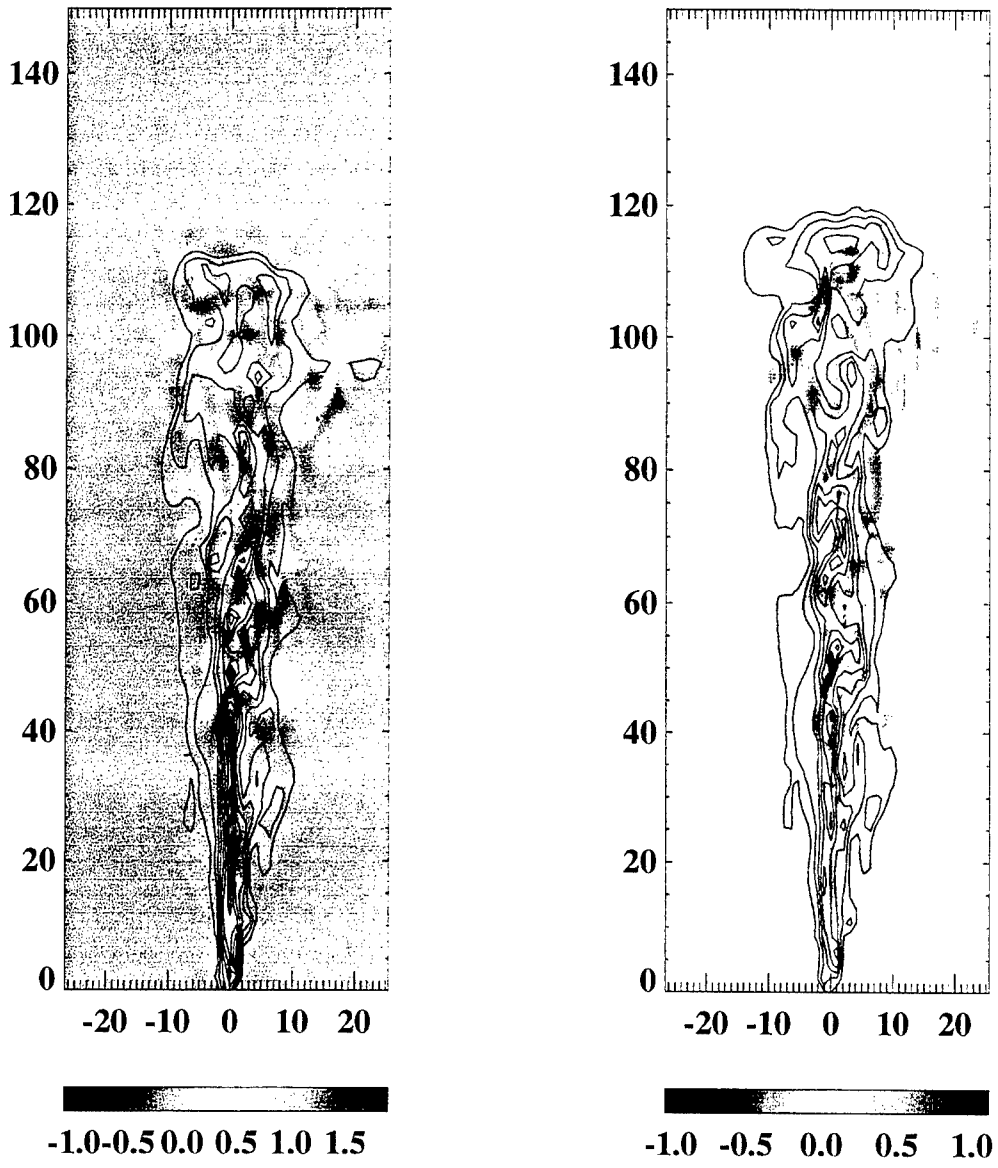

(a) 5.1 seconds

(b) 6.9 seconds

Figure 10. Gas divergence in shaded contours with dust contour lines overlaid.

4.3.2 Incompressible Phase.

Once the compressible portion of the flow was concluded, the 3D results were mapped to both axisymmetric and 3D incompressible domains. Although axisymmetry has proven to be inadequate in the compressible region, it was not clear that this would also be the case for the later stages of the flow. Since the inflow to the domain from the vent ended at roughly the 6 second mark of the compressible phase and gas velocities have dropped considerably, the problem then becomes an incompressible, buoyant, stratified, multi-phase flow.

There is some question as to where the flow should be mapped from compressible to

incompressible regimes. For steady flows, the general rule for transition to incompressible flow is that $M << 1$. The flow drops below a Mach number of 0.1 at a time of approximately 6 seconds, but the forcing continues until shortly after 6 seconds. In order to handle the inflow in a consistent manner, it was thought best to model the problem as compressible at least until the forcing from the vent was finished. The compressible portion of the simulation was run out to a time of 10 seconds and it was mapped to the incompressible regime at times of 6.9 seconds, 8.1 seconds and 10 seconds for comparison. Although the solution was not quite divergence free at the time of the mapping, the compressible solution was sufficiently convergent that the input did not destabilize the incompressible code.

Axisymmetric runs were made by averaging the 3D compressible results axially and mapping them into a domain that was 75 by 450 meters in size using resolutions of both 16 by 128 and 32 by 256. Since the domain is axisymmetric, the effective size of the simulation is 150 by 450 meters. The 3D runs utilized the same effective domain size as the axisymmetric runs and a resolution of 32 by 32 by 128 grid points.

All simulations were computed out to a time of 125 seconds after the initial blast, and the results were somewhat surprising. Plume height in the axisymmetric simulations was a strong function of mapping time, varying from nearly 400 meters when mapped at 6.9 seconds into the high resolution axisymmetric model to 270 meters when mapped from a time of 10 seconds. The axisymmetric model consistently predicted higher plume heights than did the fully 3D simulations started from any time. At higher resolutions, the axisymmetric results were even further from the 3D predictions. The reason for this appears to be the ability to resolve a tighter vortex ring at the top of the plume in the higher resolution cases. Higher resolution runs predicted a higher thinner plume than did the coarser runs from the same time, which seems to be entirely due to vortex ring at the top of the plume. While vortex rings are present in all the axisymmetric simulations, they exist only in a loose manner in the 3D simulations and break up before they can propagate very far. Figure 11 shows the predicted plume heights from high and low resolution axisymmetric runs as well as those from 3D simulations started from the three different initial conditions. Note that the high and low resolution axisymmetric runs match very well at early times before the vortex ring breaks up in the coarse resolution simulations. Also, while the 3D simulations do not vary greatly in predicted plume height, but the axisymmetric simulations are highly varied. The experimental results suggest that the plume should rise to a height of approximately 290 meters which is best matched by the axisymmetric runs mapped at a time of 8.1 seconds. Since the other axisymmetric results are so erratic, this is most likely just a coincidence. The large envelope of plume height predictions by the axisymmetric model suggest that great care should be used before settling for an axisymmetric simplification to buoyant plume flows. The relative consistency seen in the 3D simulations also suggests that the exact map over point from compressible to incompressible flow is not highly sensitive if a full 3D simulation is utilized. At least some of the difference between the height prediction by the 3D simulation and the experimental results is likely a result of inflow conditions in the compressible model. Since these conditions were provided by another model and not actual measurements, an agreement in heights between experiment and 3D simulations of less than 13% was quite acceptable.

While the axisymmetric assumption proved to be less disastrous to the solution in this phase of the problem than it was in the compressible phase, it is still not a good assumption in this flow. A

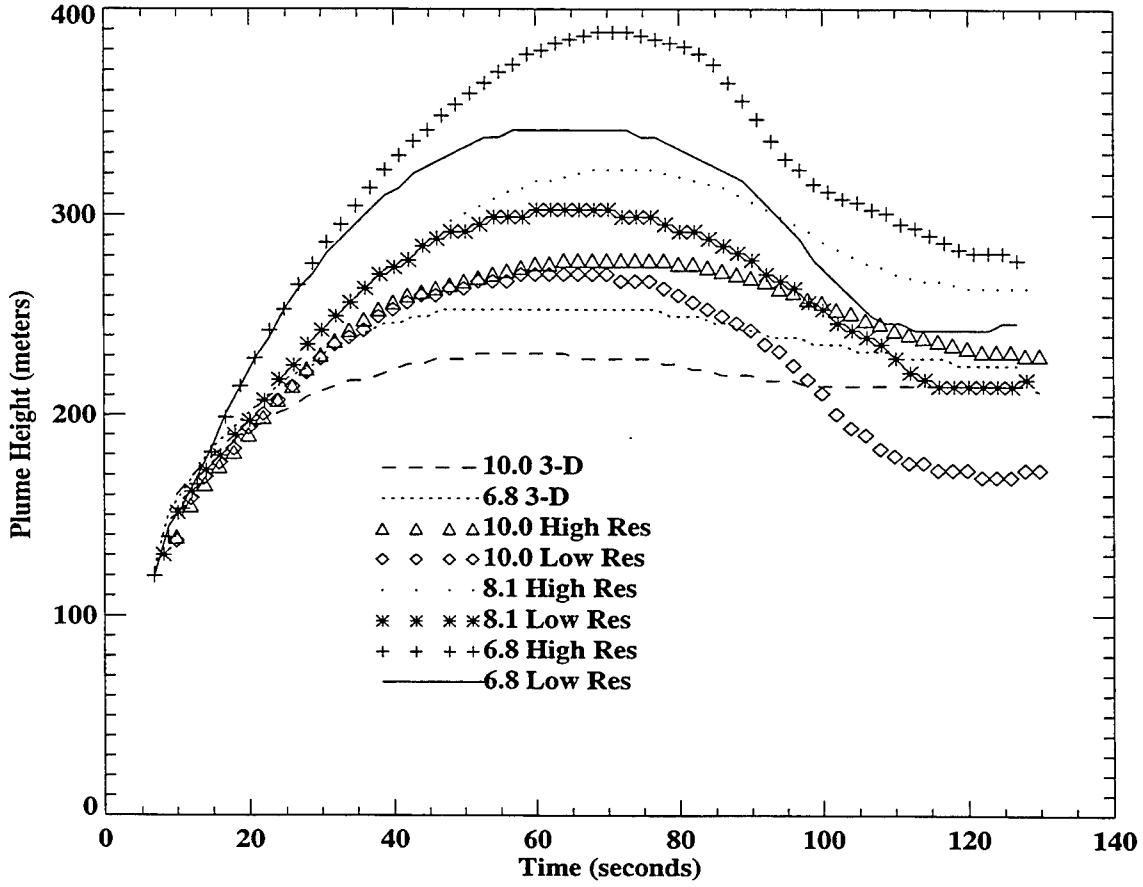

Figure 11. Plume heights predicted by axisymmetric and 3D incompressible models.

side by side comparison of frames from the low resolution axisymmetric run and the 3D run mapped from 6.9 seconds shown in Figure 12 exhibits the difference in distribution between the two simulations. The axisymmetric constraint forces the flow to move in the form of a vortices directly atop a steady plume, whereas the unconstrained 3D flow shows a vortical structure atop a generally chaotic velocity field within the plume. A series of plots from the fully 3-D simulation is show in Figure 14 and shows a very realistic evolution of the dust density over the incompressible life of the plume, spanning from the original mapping to stagnation and dust fall out.. In addition, the velocity distributions in the two simulations are quite dissimilar and lead to differences in dust distribution as well. The axisymmetric simulations tend to loft more dust to higher altitudes than do the 3D simulations keeping the dust closer to the centerline of the domain than is seen in 3D. Figure 13 shows the vertical and horizontal dust distribution in kilograms for the 3D and coarse axisymmetric models started from a time of 6.9 seconds and highlights this tendency. In particular, note the spike at the top of the axisymmetric plot of vertical distribution that shows a disproportional amount of dust in the tip of the plume.

Through comparison with experimental results and empirical models, it has been shown that plume phenomenon are not well reproduced by axisymmetric compressible models. Even with extremely high resolution, the basic physics of the problem is not represented by an axisymmetric assumption. Although the axisymmetric and 3D results agreed well in the near field region, in the far field where the plume tip was located after less than a second, only the 3D simulation was able to accurately reproduce experimental results. The plume height and spreading rate were both captured in a much better manner by a fully three dimensional model at later stages of the flow in the compressible regime. The ensemble velocity profiles of the 3D simulation fit the expected theoretical profiles to a reasonable extent, but the actual asymmetry in the flow proved to be a major contributor to the resulting plume height.

The entrainment rates observed in the compressible phase of the 3D flow were slightly lower than the rates reported by Bremhorst and Hollis [7] for near field values, but began to increase quickly in the far field. The increasing entrainment rate in the far field might suggest that increased mixing could be achieved in conventional jet flows by spreading the same volume flow through a number of smaller jets.

Finally, the incompressible phase of the flow has also proven to be poorly suited to the axisymmetric constraint. The axi-symmetry in the problem continues to predict large scale coherent structures in the flow, that are most likely not present. In addition to incorrectly capturing the velocity fields, this tendency toward coherent structures in the axisymmetric model can significantly affect the distribution of dust in a multi-phase flow. Plume height and general shape were also found to be inadequately captured with an axisymmetric model, especially when run at higher resolutions.

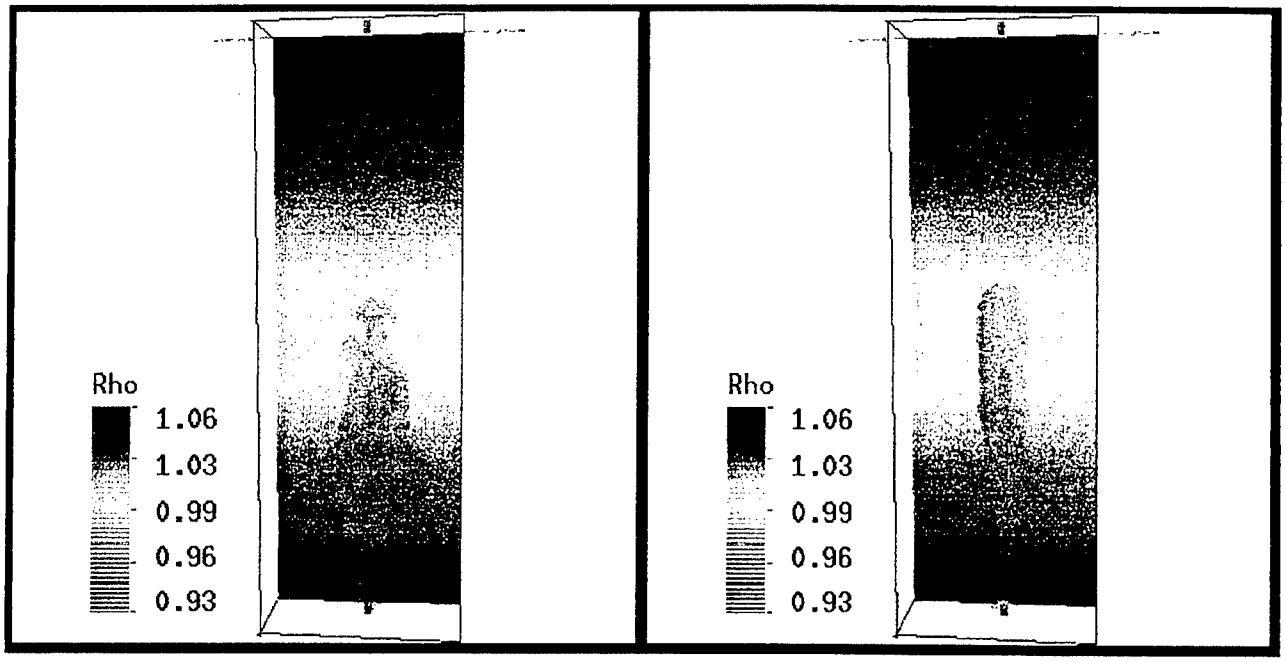

(a) Time after blast is 40 seconds.

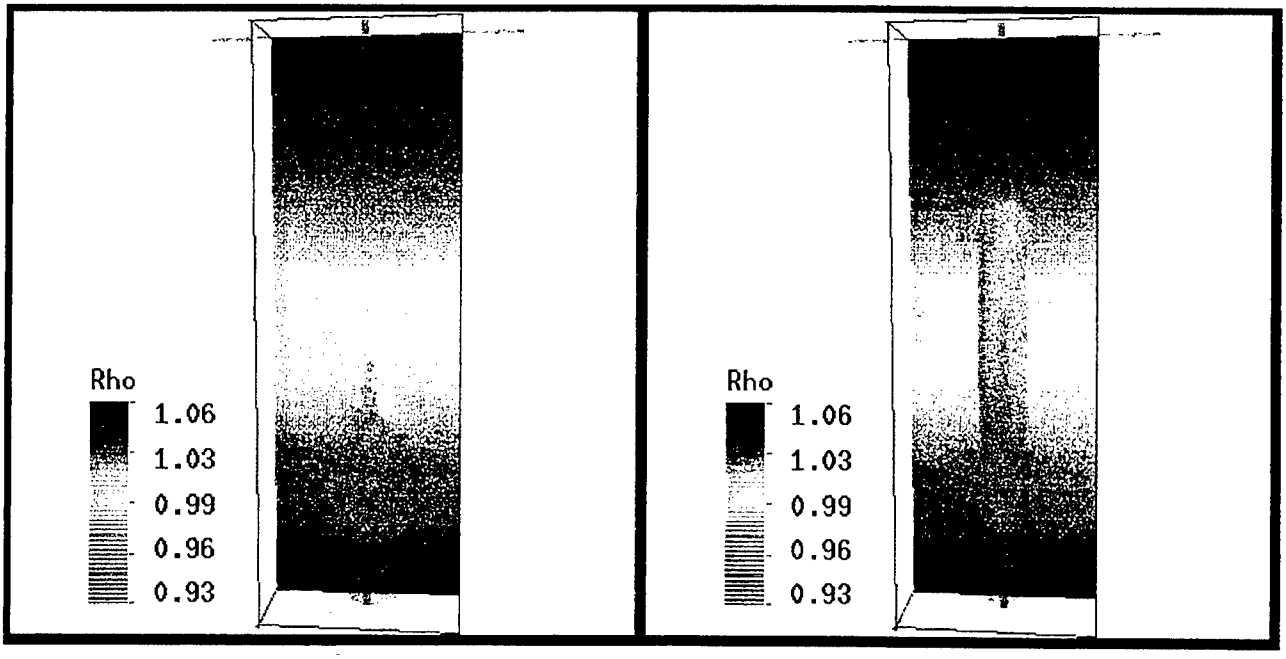

(b) Time after blast is 90 seconds.

Figure 12. Gas density in shaded contours with an isosurface of dust density in translucent blue shown from two times during the simulation. The 3D results are shown on the left and the axisymmetric results displayed in three dimensional form are on the right.

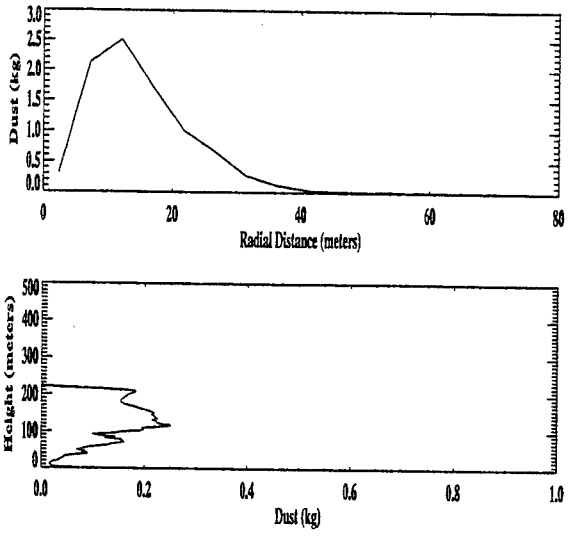

(a) 3D dust distributions

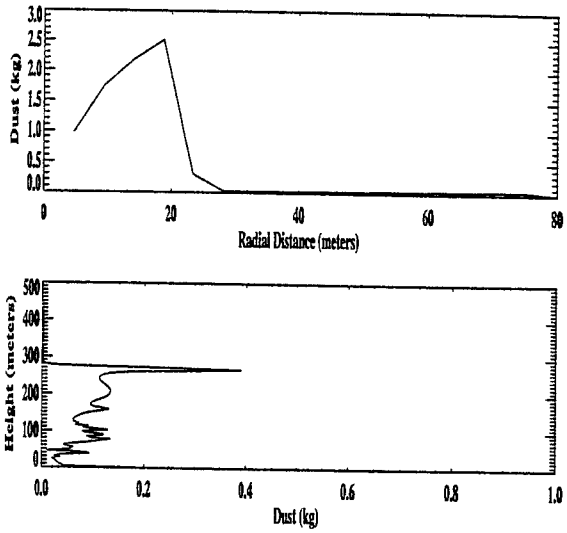

(b) Axisymmetric dust distributions

Figure 13. Horizontal (above) and vertical (below) dust distribution in 3D and axisymmetric simulations started from 6.9 seconds after the blast. These distributions are from a time of 30.8 seconds after the blast.

4.4 Unconfined Explosions.

4.4.1 Introduction.

There was very little existing data to use for comparison to simulated results presented here. STEP provides an unconfined explosion model component, but it is relatively undeveloped and was useful only to provide initial conditions to CATAPULT. The problem was mapped into the incompressible component of CATAPULT from the STEP results using a simulated dust and gas distribution. STEP output contained only a constant density component for the gas and no dust component, so gas and dust distributions similar to those in hemispherical top of a plume predicted by STEP was utilized as the initial condition.

4.4.2 Results.

Using the results from STEP for a 100 kg unconfined explosion of TNT at a height of four meters as the basis for this simulation, a buoyant bubble of gas and 1 kg of dust was mapped into CATAPULT. The simulation was conducted in axisymmetric coordinates and the results were mostly as would be expected. The bubble initially expanded slightly and then rose to a height of 85 m while slowly dissipating. All the while, dust slowly falls to the ground beneath the initial explosion. Figure 15 shows a series of plots of gas density overlain with contour lines of the log of Dust density. Given the relatively little data available for this type of explosion and the generally poor output available from STEP for unconfined explosions, our efforts were primarily focused on

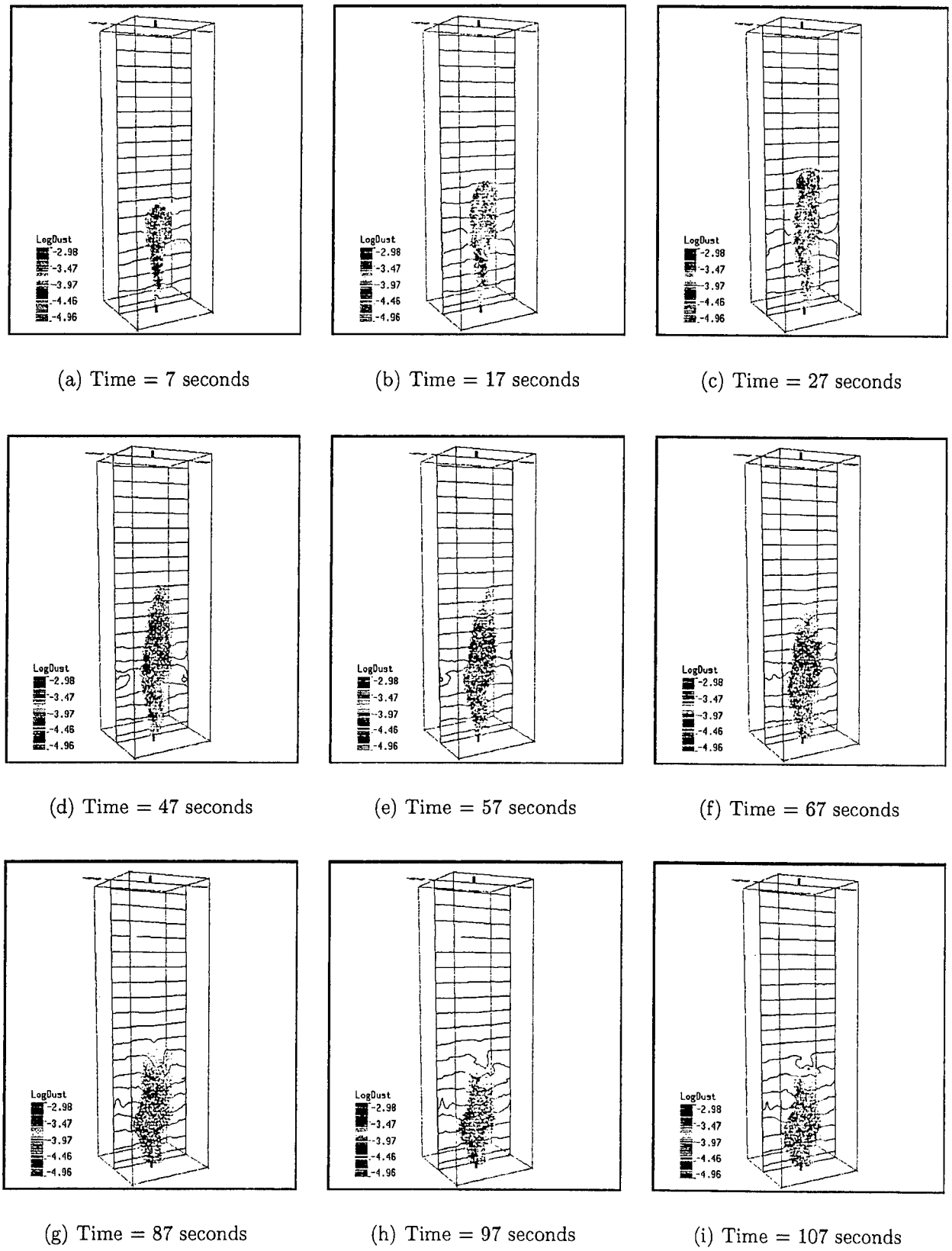

(a) Time = 7 seconds (b) Time = 17 seconds (c) Time = 27 seconds

(d) Time = 47 seconds (e) Time = 57 seconds (f) Time = 67 seconds

(g) Time = 87 seconds (h) Time = 97 seconds (i) Time = 107 seconds

Figure 14. Gas density contours (shaded) with dust density contour lines over-lain for the 3D simulation taken along a y-z cross-section from the center of the domain.

other phases of this project.

As discussed in Section 4.2, several simulations of dust bubbles in axisymmetric and 3-D coordinates were conducted and used as a validation for the 3-D component of CATAPULT. These results were remarkably similar to those observed in the unconfined explosion simulations.

4.5 Nuclear Cloud Rise Phenomena.

The late-time evolution of nuclear particulate clouds were modeled at the behest of the program director. Initial conditions were provided from two separate sources: (1) Data from MAZ computations was provided courtesy of Titan Research Technologies Corp. and (2) data from SHARC computations was provided courtesy of Maxwell Technologies, Inc.

Two-dimensional axisymmetric computations are performed for a 500 ton surface burst for a computational domain of 1000x3000 meters. The initial data is mapped from a two-dimensional axisymmetric compressible computation from MAZ. The MAZ computation simulates the cloud evolution for a period of 0-60 seconds after burst. Care must be taken to ensure that data used from the compressible computation is at an effectively incompressible state throughout the flow field. Three flow field criteria are used to determine the time when the flow is sufficiently incompressible: (1) an absence of shock waves, (2) a sufficiently low Mach number, and (3) a sufficiently low velocity divergence. Although the shock wave from the initial blast leaves the domain of interest at a very early time, the Mach number and velocities remain high for several seconds. At 20 seconds after blast, the maximum Mach number present in the flow field is M_{max} = 0.65 and the average Mach number (averaged for grid points having $M > 0.1$) is $M_{avg} = 0.30$. At 60 seconds the maximum Mach number is decreased to M_{max}= 0.48 and the average Mach number is decreased to M_{avg}= 0.25. A contour plot of the velocity diverge calculated using centered differences is shown in Figure 16 for the 20 and 60 second times. Figure 16a indicates a sizable region of compressible flow located in the rising fireball with a maximum velocity divergence of $\nabla \cdot u = 0.1635 s^{-1}$. At 60 seconds the flow field is largely incompressible as indicated in Figure 16b where the maximum divergence $\nabla \cdot u = 0.035 s^{-1}$ is decreased nearly an order of magnitude from that of Figure 16 a.

As expected, attempting to advance the solution with the present method using initial data that has regions of compressible flow is found to cause numerical instabilities. The evolution of the density fields for both the gas-phase and particle-phase computed from the multiphase projection method are shown in Figure 17 for the 500 ton surface burst described above. The initial condition is mapped from MAZ results at 60 seconds after blast (AB). Nine frames depict the evolution of the nuclear cloud for the times indicated on each frame in Figure 17. The solution is advanced for six minutes, or 420 seconds AB. This required approximately 8 hours of CPU time on a Pentium II 400 MHz processor for 32x128 grid points. The color scale depicts the density ρ of the gas-phase which indicates the atmospheric stratification of the air, where redder shades indicate higher densities. The contour lines depict the log of the dust-particle density ρ. The specified particle diameter of 60 microns is determined by calculating the mass-weighted average for eight particle groups present in the upper cloud of the MAZ computation. The dust contours of the initial condition depicted in the 60 second frame of Figure 17 shows the major structures

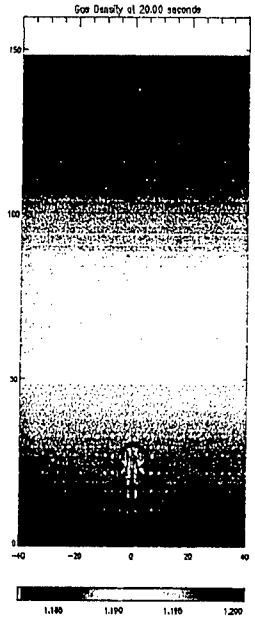

(a) Time = 10 seconds

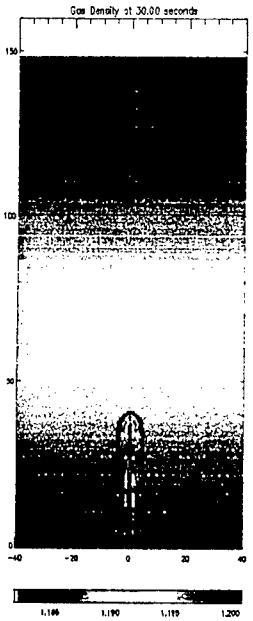

(b) Time = 20 seconds

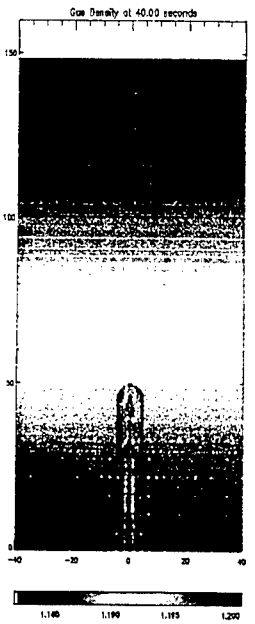

(c) Time = 30 seconds

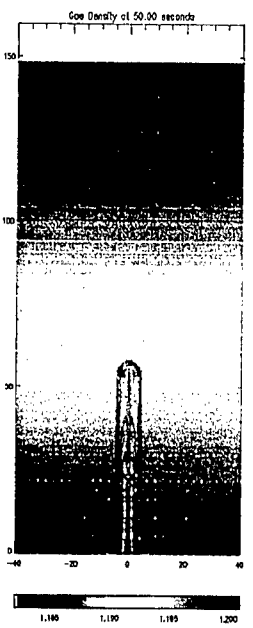

(d) Time = 40 seconds

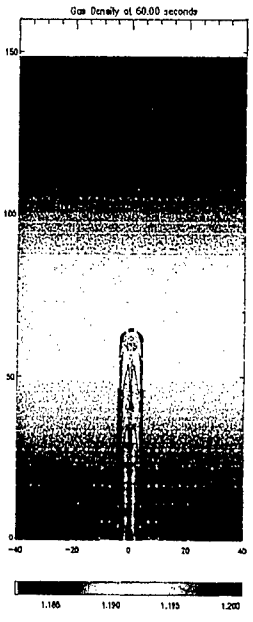

(e) Time = 50 seconds

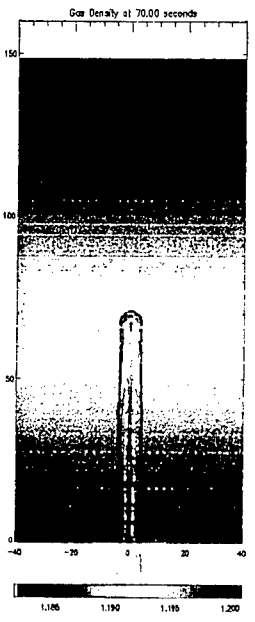

(f) Time = 60 seconds

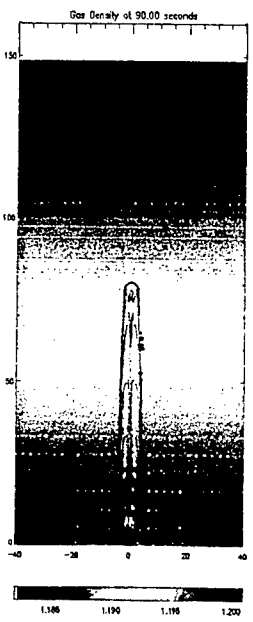

(g) Time = 80 seconds

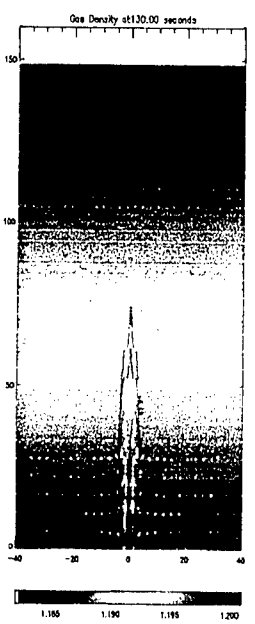

(h) Time = 120 seconds

Figure 15. Gas density contours (color) with dust density contour lines over-lain for the axisymmetric simulation of an unconfined explosion.

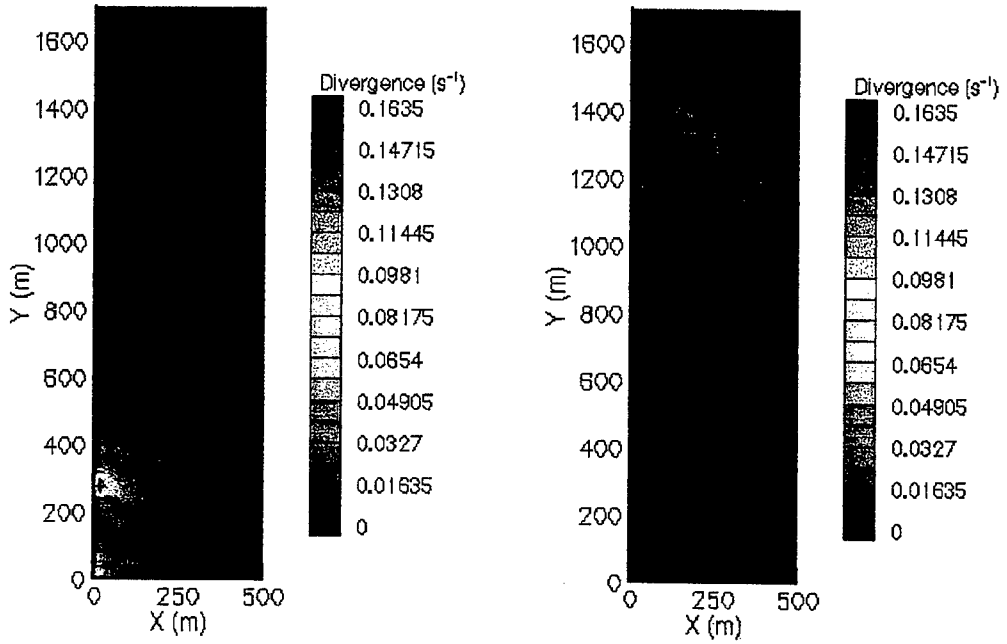

(a) 20 seconds

(b) 60 seconds

Figure 16. Velocity divergence for a nuclear cloud-rise simulation computed from MAZ at (a) 20 seconds after burst, and (b) 60 seconds after burst. The divergence at 60 seconds has decreased by an order of magnitude from that at 20 seconds indication a flow field that is much more incompressible.

typical to nuclear clouds, consisting of the pedestal, stem, and the cloud-top.[1] The shade of the cloud top is much lighter than that of the surrounding atmosphere, which indicates that the fireball has a lower density than that of the ambient air.

The top of the cloud initially rises due to both the initial upward momentum of the cloud and the buoyancy of the cloud created by low density in the cloud-top. Both dust and the high-density air at the lower altitude are entrained into the toroidal vortex as the cloud rises into the stratified atmosphere as shown in the 108 second frame in Figure 17b. After reaching a maximum height of around 1900 meters, the high-density air that is convected to high altitudes by the cloud begins fall back toward ground as shown in Figure 17c. This results in the convection of low-density air in the upper atmosphere to lower altitudes, indicated by the gas density field in Figure 17d. The low-density air then "bounces" back into the upper altitudes once again entraining high-density air to higher altitudes and driving the cloud top upwards to reach a maximum altitude at over 2100 meters (Figures 17(e-g)). The gas phase then begins a second oscillation as indicated in Figures 16(h-i).

While the dust-phase is shown to generally mirror the movement of the gas-phase, the dust is also observed to fall toward the lower boundary due the gravity force. This effect is observed by the movement of the dust density contours near the bottom of the stem. The dust-phase in the cloud-top is also observed to spread in the radial direction via the main toroidal vortex as well as a secondary vortex created by the oscillation of the gas-phase. Oscillating phenomena such as that observed in the computation described above are well known in the field of meteorology as atmospheric gravity waves. A parcel of fluid vertically displaced from its equilibrium position in a region of stable stratification will oscillate at a frequency that is a function of the vertical density gradient. This frequency is called the Brunt-Väsällä frequency and can be approximated as follows[23],

$$N^2 \approx g\left[-\frac{1}{\rho}\frac{\partial \rho}{\partial y}\right]. \tag{12}$$

The frequency for the present case is calculated to be $4.835x10^{-3}$ Hz, or a period of 207 seconds, using a linear approximation of the density gradient over the range of the maximum cloud-height and the average density of the gradient for Eq. 12. This calculated value is in good agreement with the period of 198 seconds observed in the computation.

Sensitivity of the specified particle diameter d is demonstrated by the computation shown in Figure 18. Here, the particle diameter for the same 500 ton surface burst is specified to be 200 microns, determined by a mass average of the particle phase from the MAZ data that now includes particles in the pedestal and stem of the cloud. The 200 micron cloud in Figure 18 evolves much in the same manner as the 60 micron cloud in Figure 17. However, due to the increased mass and inertia of the individual particles, the cloud achieves a maximum altitude of approximately 1900 meters, 200 meters less than the case in Figure 2. Due to a higher terminal velocity, the 200 micron particle-phase is also observed to fall out much more quickly than the 60 micron case as indicated by absence of the cloud pedestal in Figures 18(d-i) as well as the movement of the dust contours in the cloud stem.

A nuclear cloud-rise simulation using SHARC data as the initial condition is also performed to

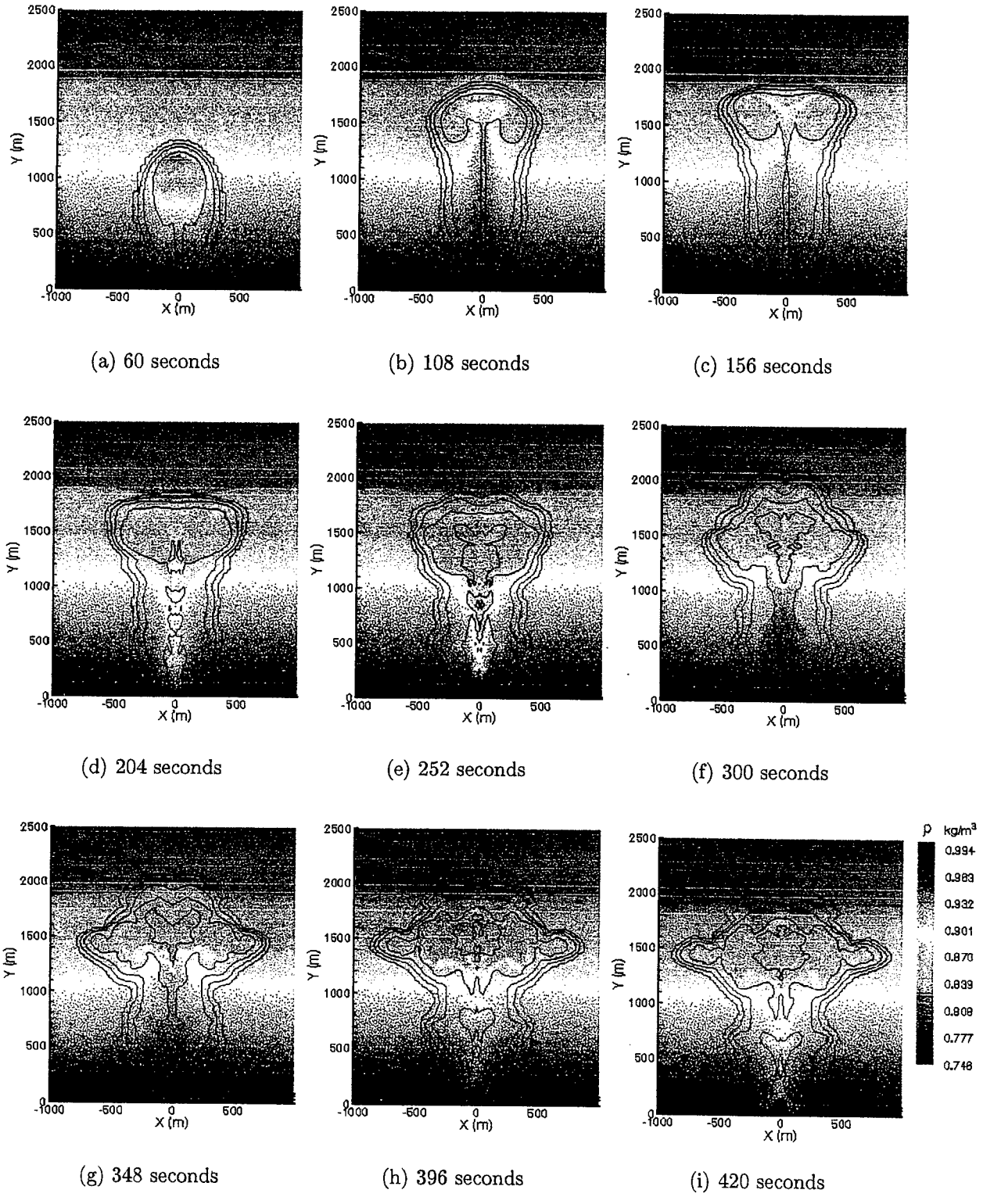

(a) 60 seconds (b) 108 seconds (c) 156 seconds

(d) 204 seconds (e) 252 seconds (f) 300 seconds

(g) 348 seconds (h) 396 seconds (i) 420 seconds

Figure 17. Nuclear cloud-rise simulation computed from the multiphase projection methods for a particle diameter of 60 microns. Initial conditions are remapped from MAZ results at 60 seconds after a 500 ton surface burst.

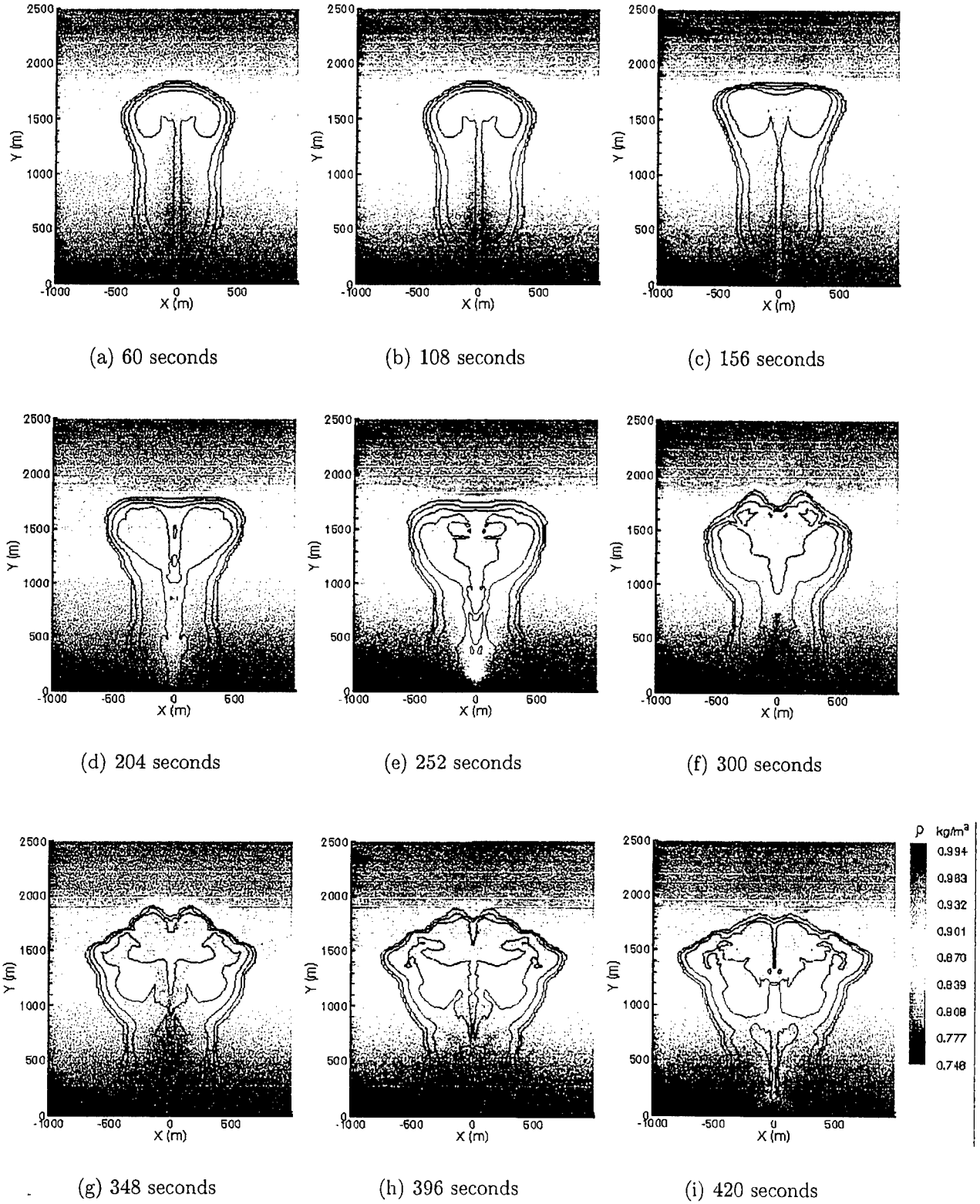

(a) 60 seconds (b) 108 seconds (c) 156 seconds

(d) 204 seconds (e) 252 seconds (f) 300 seconds

(g) 348 seconds (h) 396 seconds (i) 420 seconds

Figure 18. Nuclear cloud-rise simulation computed from the multiphase projection method for a particle diameter of 200 microns. Initial conditions are remapped from MAZ results at 60 seconds after a 500 ton surface burst.

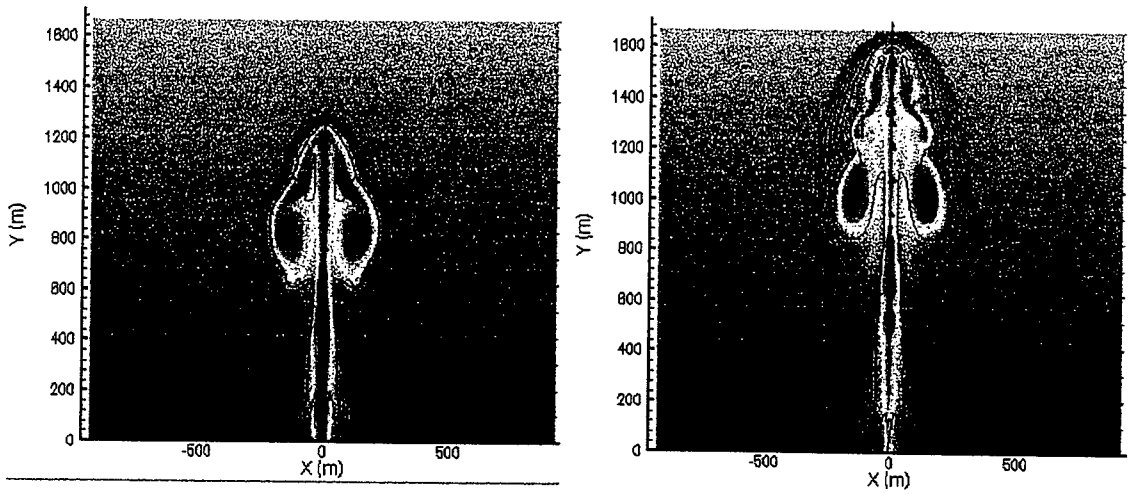

(a) 0 seconds

(b) 25.8 seconds

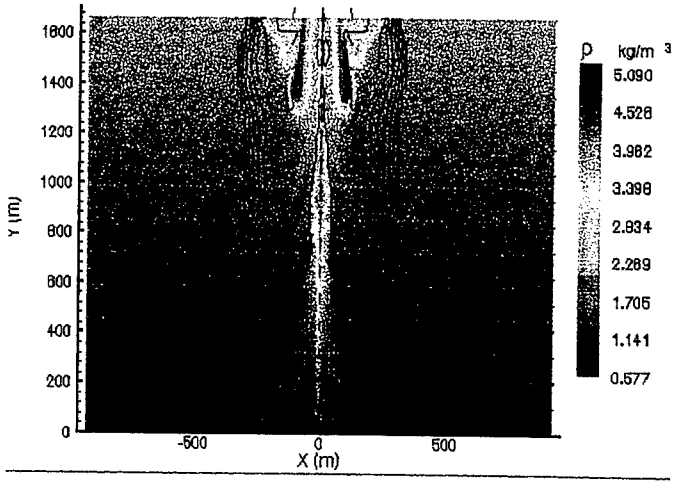

(c) 32.6 seconds

Figure 19. Nuclear cloud-rise simulation computed from the multiphase projection method for a particle diameter of 100 microns. Initial conditions are remapped from SHARC results at 50 seconds after a 10 kiloton surface burst.

demonstrate the versatility of the projection scheme to advance flow field solutions for a variety of compressible data. Figure 19(a) shows the nuclear cloud data obtained from SHARC for a 10 kiloton yield at a height of burst of 30 meters 23 seconds after burst. The particle diameter is specified to be 100 microns. Similar to Figures 17 and 18, the color scale depicts the gas density while the black contour lines show the log of the particle density. In the same manner as the computations started from the MAZ data in Figures 16, the low density fire rises due to both buoyancy and initial upward momentum. The cloud-top exits the computational domain as shown in Figure 19(c). For this case, the vertical dimension of the physical domain is too small to observe the oscillation phenomena present in the cases shown in Figures 17-18.

The case for the 500 kiloton surface burst with 60 micron particles shown in Figure 18 is mapped onto a coarse three-dimensional grid and advanced out to 138 seconds after blast shown in Figure 20. The initial flow field is shown in Figure 20(a) where the blue surface represents the $10^{-06} kg/m^3$ isosurface of the dust density and the black contour lines show the gas density. The grid resolution is 32x32x64 for a domain of 2000x2000x2500 meters and required approximately 24 hours to run on a 400 MHz Pentium II processor. Similar to the trend observed with the confined plumes described in section 4.3.2, the three-dimensional cloud reaches a maximum height much lower than the axisymmetric case, approximately 1750 meters shown in Figure 20(b) at 78 seconds after burst as compared to 2100 meters in Figure 18. In the same manner as the axisymmetric case the high density gas and entrained dust fall back toward the lower boundary shown in Figure 20(c).

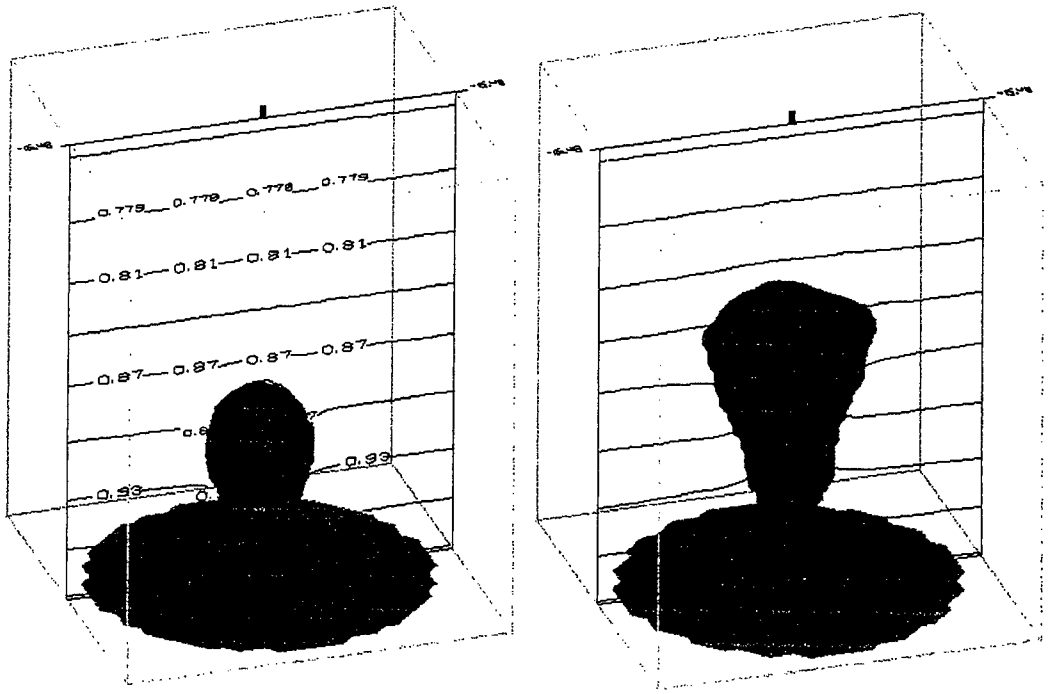

(a) 0 seconds

(b) 25.8 seconds

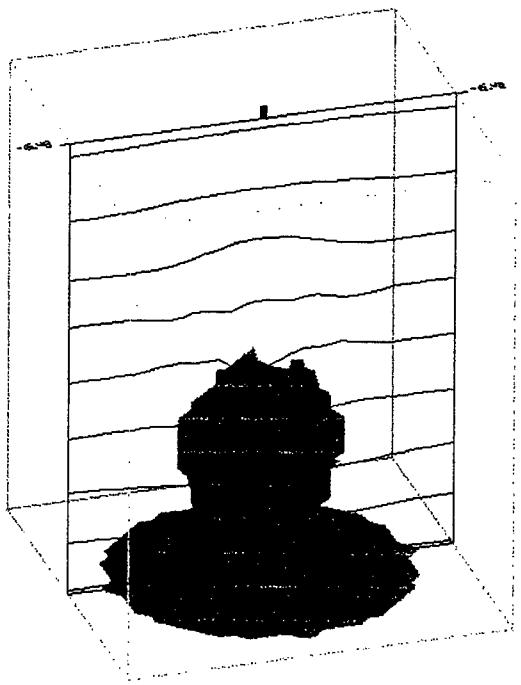

(c) 32.6 seconds

Figure 20. 3-D nuclear cloud-rise simulation computed from the multiphase projection method for a particle diameter of 100 microns. Initial conditions are remapped from TRT data.

Section 5
Conclusions

The overall objective of this effort was to develop, implement, and demonstrate high resolution computer codes to simulate multiphase reactive flow fields associated with cloud-rise phenomenology. These codes are important to DTRA interests and are applicable to a broad range of DTRA and defense applications, particularly post-explosion environments for nuclear, biological, and chemical (NBC) weapons. Such codes also have potential commercial application and nonmilitary benefits since multiphase particulate flows are also encountered in numerous industrial settings.

To meet the overall objective, KTI has developed a high performance numerical modeling software package named the Computational All-Time Algorithm Package with Underlying Lawrence Technology (CATAPULT) for the numerical simulation of compressible and incompressible multiphase flows. "All-Time" indicates CATAPULT's capability to model flows in both the compressible and incompressible time scales. Having both compressible and incompressible flow solver modules provide an efficient method to advance solutions for transient flows that are compressible at early times and incompressible at later times. CATAPULT incorporates the latest technologies in high-order Godunov (HOG) schemes and projection methods and has the capability to handle two-dimensional planar, axisymmetric, and full three-dimensional computations.

The development and utilization of CATAPULT has resulted in an increased understanding of post-explosion environments both in terms of the physical processes involved and the issues that arise in developing accurate models for such environments. The technology and knowledge resulting from this effort serve as a significant step towards the future development of sophisticated, accurate, and fast computational tools that will further the knowledge of multiphase, particulate flow field environments. The following subsections give a brief review of the developments and findings in this study, a discussion on the extent to which the objectives were achieved, and the work required to develop the technology further.

5.1 Results.

The CATAPULT software was developed and assembled based on the suite of advanced numerical schemes developed by the research group at LBNL. The compressible flow module consists of the scheme developed by Collins et al. [12] and is tailored to simulate NBC cloud-rise scenarios.

The incompressible flow module was developed that incorporates a particle-phase model like that in Collins et al.[12] with the projection method of Bell et al. [5]. The solution method for the governing gas-phase equations is modified with an intermediate projection as described in [3] and the solution for the governing particle-phase equations is modified with unsplit Godunov scheme for the particle equations as described in [9]. The rate of convergence for the resulting multiphase projection method indicates second-order accuracy for the gas phase and between first and second-order accuracy for the particle-phase.

CATAPULT was used to investigate plumes resulting from confined explosions. Through

comparison with experimental results and empirical models, it has been shown that plume phenomena are not well reproduced by axisymmetric compressible models. Even with extremely high resolution, the basic physics of the problem is not represented by an axisymmetric assumption. Although the axisymmetric and 3D results agreed well in the near field region, in the far field where the plume tip was located after less than a second, only the 3D simulation was able to accurately reproduce experimental results. The plume height and spreading rate were both captured in a much better manner by a fully three dimensional model at later stages of the flow in the compressible regime. The ensemble velocity profiles of the 3D simulation fit the expected theoretical profiles to a reasonable extent, but the actual asymmetry in the flow proved to be a major contributor to the resulting plume height.

The entrainment rates observed in the compressible phase of the 3D flow were slightly lower than the rates reported by Bremhorst and Hollis [7] for near field values, but began to increase quickly in the far field. The linear trend of plume height versus the square root of non-dimensional time was observed during the early phase of the compressible problem, but did not persist until the vent velocity reached zero. The findings of this study indicate that the results from previous jet flow researchers are applicable to multi-phase plumes in the near field region. However, as the flow expanded away from the near field to distances greater than 100 d_0, the plume characteristics generally began to diverge from jet characteristics as entrainment rates increased and plume tip penetration slowed.

Finally, the incompressible phase of the flow has also proven to be poorly suited to the axisymmetric constraint. The axisymmetry in the problem continues to predict large scale coherent structures in the flow, that are most likely not present. In addition to incorrectly capturing the velocity fields, this tendency toward coherent structures in the axisymmetric model can significantly affect the distribution of dust in a multi-phase flow. Plume height and general shape were also found to be inadequately captured with an axisymmetric model, especially when run at higher resolutions.

Multiphase particulate clouds resulting from unconfined explosions were also simulated. There is very little existing data for unconfined explosions that can be used for comparison and as initial conditions for the simulations. Thus, the unconfined simulations in this effort are limited to the output of the unconfined explosion model component of STEP, which is relatively undeveloped as well. While axisymmetric and three-dimensional simulations appear to qualitatively capture the large-scale dynamics, more detailed initial conditions are required to obtain more quantitatively accurate unconfined simulations.

Cloud-rises resulting from nuclear blasts for the incompressible time-scales were simulated at the behest of the program director. Initial conditions were obtained from two different hydrocodes that have been used to simulate the compressible time scale of nuclear blasts. MAZ data was provided courtesy of TRT and SHARC data was provided courtesy of Maxwell Technologies. Data from both sources were successfully mapped into the incompressible module of CATAPULT and advanced to later (incompressible) times.

An example of one such case is the computation of an axisymmetric cloud evolution for a 500 ton surface burst. The computation is initialized using MAZ flow field data at 60 seconds after burst. The 60 second flow field is determined to be incompressible and, therefore, appropriate to begin

the projection calculation. The solution is advanced out to a time of six minutes from the initial condition and accurately captures the large scale structure of the cloud evolution, including the Brunt-Väsällä oscillation. The maximum altitude obtained by the cloud and the rate of fall out for the particle-phase is found to be sensitive to the specified particle diameter.

5.2 Progress vs. Proposed Objectives.

The objectives listed in the Phase II proposal are restated below:

Technical Objective 1: Simulate gas-particle cloud rise resulting from the compromise of a confined CB facility. Analyze the results and compare with experimental data and/or other models as available.

Technical Objective 2: Simulate gas-particle cloud rise resulting from the compromise of an unconfined CB facility. Analyze the results and compare with experimental data and/or other models as available.

Technical Objective 3: Modify, implement, and optimize algorithms, schemes, and codes and/or other models as available.

The first objective was achieved through the development of CATAPULT to simulate both the compressible and incompressible time-scales of a confined scenario. Knowledge and understanding of the physical processes and issues of modeling were garnered through comparisons with experiments, i.e., the Dipole East 159 [2] and (jet experiments from the literature), as well as results from STEP.

The second objective was partially achieved through CATAPULT simulations for the incompressible time-scale of an unconfined event. Initial conditions were limited to the relatively undeveloped unconfined explosion module of STEP. Experimental data was not available for comparison.

The third objective was fully achieved through the developments of CATAPULT described in the first two paragraphs in the previous sub-section.

5.3 Future Work.

The CATAPULT code developed under this contract is a significant addition to the modeling capabilities of DTRA. In order to become a useful operational tool however, some further work is required. The dust phase of flow in CATAPULT is currently assumed to consist of dust particles of constant size. Modeling the dust using multiple particle sizes would increase the capabilities of the code significantly. This could be accomplished in several ways and some study would be required to determine the most effective method. Also, in order to correctly model nuclear cloud rise phenomena, the addition of thermodynamic coupling to the code would be required. Most nuclear clouds contain large amounts of water vapor that cool and condense as it is entrained to

higher altitudes. This condensation releases a significant amount of latent heat that contributes further to the energy and buoyancy of the cloud. In order to model nuclear cloud rise events in most environment, it is essential that thermodynamics be included in the model. Other physics prominent in NBC post-explosion environments should also be incorporated into the model including non-dilute regions of particulates and chemical reactions.

Perhaps the most important improvement required to make CATAPULT a useful *operational* tool is code parallelization. Three dimensional computations of plume phenomenon from confined explosions required approximately two months to run to completion on Cray vector computers and PC's. Code parallelization would allow CATAPULT to run a similar simulation to completion in 12 to 36 hours on a typical Cray T3E machine, and make operational use of the code highly feasible. The technology necessary to accomplish code parallelization currently exists and is relatively uncomplicated to implement, although it does require a significant effort in terms of manpower and computer resources to test and validate.

Section 6
References

[1] Nuclear Particulate Clouds. DNA technical report, 1992. DNA-EM-1-CH-4.

[2] C. Allen, R. Jellerson, H. Edwards, and W. Espander. Optical Data From Dipole East 159 For The Collateral Effects Program. Technical report, Logicon R&D Associates, 1997. Technical Report to the Defense Special Weapons Agency.

[3] A. S. Almgren, J. B. Bell, P. Collela, L. H. Howell, and M. L. Welcome. A Conservatie Adaptive Projection Method For The Variable Density Incompressible Navier-Stokes Equations. Lbnl internal report, 1996. LBLN-39075.

[4] N. Atassi, J. Boree, and G. Charnay. Transient Behavior Of An Axisymmetric Turbulent Jet. *Applied Scientific Research*, 51:137–143, 1993.

[5] J. B. Bell, P. Colella, and H. M. Glaz. A Second-Order Projection Method For The Incompressible Navier-Stokes Equations. *Journal of Computational Physics*, 85:257–283, 1989.

[6] J. B. Bell and D. L. Marcus. A Second-Order Projection Method For Variable-Density Flows. *Journal of Computational Physics*, 101:334–348, 1992.

[7] K. Bremhorst and P.G. Hollis. Velocity Field Of An Axisymmetric Pulsed, Subsonic Air Jet. *AIAA Journal*, 28(12):2043–2049, December 1990.

[8] B. P. Brown, M. A. Potts, and J. Krispin. Projection Methods For Incompressible Multiphase Cloud-Rise Phenomena. AIAA Paper 99-3321, 1999. In 14th AIAA Computational Fluid Dynamics Conference Proceedings.

[9] X. Q. Chen and J. C. f. Pereira. Eulerian-Eulerian Predictions Of Dilute Turbulent Gas-Particle Flows. *FED*, 228:265–272, 1995.

[10] A. Chorin. Numerical Solution Of The Navier-Stokes Equations. *Math. Comp.*, 22:742–762, 1968.

[11] P. Colella. Multidimensional Upwind Methods For Hyperbolic Conservation Laws. *Journal of Computational Physics*, 87:171–200, 1990.

[12] J.P. Collins, R.E. Ferguson, K. Chien, A.L. Kuhl, J. Krispin, and H.M. Glaz. Simulation Of Shock-Induced Dusty Gas Flows Using Various Models. AIAA Paper 94-2309, 1994. In 25th AIAA Fluid Dynamics Conference Proceedings.

[13] S. Godoy, A. D. Gosman, and P. Hutchinson. Droplet Motion In Turbulent Flows. *FED-Gas Solid Flows*, 10:31–35, 1984.

[14] S. Hikida, K. Peterson, T. Pierce, R. Seebaugh, and J. Simmons. Chem/Bio Source Model Step 2.3 User's Manual. Technical report, Applied Research Associates, 1998. Technical Report to the Defense Special Weapons Agency.

[15] H. Johari, Q. Zhang, M.J. Rose, and S.M. Bourque. Impulsively Started Turbulent Jets. *AIAA Journal*, 35(4):657–662, April 1997.

[16] H. Kouros, R. Medina, and H. Johari. Spreading Rate Of An Unsteady Turbulent Jet. *AIAA Journal*, 31(8):1524–1526, 1993.

[17] J. Krispin. High-order godunov schemes for multiphase flows. Final Report KTI TR 97-1, 1997. Contract No. DSWA01-96-C-0125.

[18] J. Krispin, J. P. Collins, and H. M. Glaz. High-resolution solutions of stiff chemically reacting flows. *Journal of Thermophysics and Heat Transfer*, 10:570–578, 1996.

[19] J. Krispin and J.P. Collins. Simulations of dusty flows in an incompressible gas using the projection method. AIAA Paper 95-2164, 1995. In 26th AIAA Fluid Dynamics Conference Proceedings.

[20] J. Krispin and H. M. Glaz. Nonequilibrium, chemically reacting flowfields and the implicit-explicit godunov scheme. Proc. 13th international conference on numerical methods in fluid dynamics, rome, italy, 1992. eds. M. Napolitano and F Sabetta, Springer-Verlag.

[21] E.K. Longmire and J.K.Eaton. Structure of a particle-laden round jet. *Journal of Fluid Mechanics*, 236:217–257, 1992.

[22] H. Miura and I. I. Glass. On the passage of a shock wave through a dusty-gas layer. *Journal of Computational Physics*, 87:171–200, 1990.

[23] S. Pond and G. L. Pickard. *Introduction to Dynamical Oceanography.* Butterworth Heinemann, 1995. 2nd Edition.

[24] M. A. Potts, B. P. Brown, J. Krispin, J. P. Collins, and R. E. Ferguson. Two phase plume dynamics–a comparison of axisymmetric and three dimensional simulations. AIAA Paper 99-3764, 1999. In 30th AIAA Fluid Dynamics Conference and Exhibit Proceedings.

[25] F. M. White. Incompressible turbulent mean flow. In *Viscous Fluid Flow, 2nd Edition*, pages 472–476. McGraw-Hill, Inc., New York, 1991.

[26] J. C. Wilson. The drag force experienced by spherical particles in accelerated, rectilinear motion of reynolds numbers as large as 70. *FED-Gas Solid Flows*, 10, 1984.

DISTRIBUTION LIST

DEPARTMENT OF DEFENSE

DEFENSE TECHNICAL INFORMATION CENTER
8725 JOHN J.KINGMAN ROAD, SUITE 0944
FORT BELVOIR, VA 22060-6218
ATTN: DTIC/OCP

DEFENSE THREAT REDUCTION AGENCY
6801 TELEGRAPH ROAD
ALEXANDRIA, VA 22310-3398
ATTN: CPF
ATTN: CPOH, D. BRUDER
ATTN: CPOH, DR P. CASTLEBERRY
ATTN: CPW
ATTN: CPWE, L. WITTWER
ATTN: CPWP, DR M.FRANKEL
ATTN: CPWP, DR K. SCHWARTZ
ATTN: CPWPT/TECHNICAL RESOURCE CENTER
ATTN: CPWS, D. SUNSHINE
ATTN: CPWT, DR K. KIM
ATTN: NSSA, J. URBAN

DEFENSE THREAT REDUCTION AGENCY
ALBUQUERQUE OPERATIONS
1680 TEXAS STREET, SE
KIRTLAND AFB, NM 87117-5669
ATTN: CPT, DR G. BALADI
ATTN: CPTN, DR E. RINEHART
ATTN: CPTO
ATTN: CPTP, E. MARTINEZ
ATTN: CPTP, J. HUGHES

USSTRATCOM/J531T
901 SAC BOULEVARD, SUITE BB11
OFFUTT AFB, NE 68113-5160
ATTN: LTCOL J. SMITH

DEPARTMENT OF DEFENSE CONTRACTORS

AEROSPACE CORPORATION
P. O. BOX 92957
LOS ANGELES, CA 90009-2957
ATTN: H. MIRELS, M5-741
ATTN: LIBRARY ACQUISITION, M1/199

APPLIED RESEARCH ASSOCIATES, INC.
4300 SAN MATEO BOULEVARD, NE, SUITE A220
ALBUQUERQUE, NM 87110-1260
ATTN: R. NEWELL

ARES CORPORATION
1800 NORTH KENT STREET, SUITE 1230
ARLINGTON, VA 22209
ATTN: A. DEVERILL
ATTN: R. LOCKE

CHARLES NEEDHAM
1424 HERTZ DRIVE, SE
ALBUQUERQUE, NM 87108
ATTN: C. NEEDHAM

EASTWIND RESEARCH CORP
P. O. BOX 13081
BELMONT SHORE, CA 90803-8081
ATTN: R. D. SMALL

GEO CENTERS, INC.
P. O. BOX 428
NEWTON UPPER FALLS, MA 02164
ATTN: B. NELSON

INFORMATION SCIENCE, INC.
1390 CAMINO MANADERO
SANTA BARBARA, CA 93111-1048
ATTN: W. DUDZIAK

ITT INDUSTRIES
ITT SYSTEMS CORPORATION
ATTN: AODTRA/DTRIAC
1680 TEXAS STREET, SE
KIRTLAND AFB, NM 87117-5669
ATTN: DTRIAC
ATTN: DTRIAC/DARE

ITT SYSTEMS & SCIENCES CORPORATION
P. O. BOX 15012
COLORADO SPRINGS, CO 80935-5012
ATTN: J. KEITH

ITT SYSTEMS CORPORATION
2560 HUNTINGTON AVENUE
ALEXANDRIA, VA 22303
ATTN: R. GUENTHER

JAYCOR
1410 SPRING HILL ROAD, SUITE 300
MCLEAN, VA 22102
ATTN: DR C. P. KNOWLES

KRISPIN TECHNOLOGIES, INC
1370 PICCARD DR, SUITE 210
ROCKVILLE, MD 20850
ATTN: B. BROWN
ATTN: J. KRISPIN
ATTN: J. COLLINS
ATTN: M. POTTS
ATTN: R. FERGUSON

KTECH CORPORATION
2201 BUENA VISTA DRIVE, SE, SUITE 400
ALBUQUERQUE, NM 87106-4265
ATTN: D. JOHNSON

LOCKHEED MARTIN CORPORATION
P. O. BOX 3504
SUNNYVALE, CA 94088-3504
ATTN: TECH INFO CTR D/COLL,
D/90-11, B/106

LOCKHEED MARTIN VOUGHT SYSTEMS
P. O. BOX 650003
DALLAS, TX 75265-0003
ATTN: LIBRARY EM-08

LOGICON ADVANCED TECHNOLOGY
6053 WEST CENTURY BOULEVARD
LOS ANGELES, CA 90045-6430
ATTN: B. LEE
ATTN: D. SIMONS
ATTN: G. IVY
ATTN: G. WALSH

LOGICON INC.
LOGICON ADVANCED TECHNOLOGY
P.O. BOX 471
SAN PEDRO, CA 90733-0471
ATTN: INFORMATION CENTER

LOGICON - RDA
6940 S. KINGS HIGHWAY, SUITE 202
ALEXANDRIA, VA 22310
ATTN: R POPE

LOGICON - RDA
P. O. BOX 9377
ALBUQUERQUE, NM 87119-9377
ATTN: F. ROESSLER
ATTN: G. GANONG
ATTN: J. RENICK

LOGICON, INC.
LOGICON ADVANCED TECHNOLOGY
P. O. BOX 471
SAN PEDRO, CA 90733-0471
ATTN: LIBRARY

MAXWELL TECHNOLOGIES, INC.
FEDERAL DIVISION
8888 BALBOA AVENUE
SAN DIEGO, CA 92123-1506
ATTN: C. PETERSEN
ATTN: DR C. WILSON
ATTN: G. SCHNEYER
ATTN: J. BARTHEL
ATTN: J. MURPHY
ATTN: LIBRARY
ATTN: P. COLEMAN
ATTN: S. ROGERS
ATTN: T. PIERCE

MAXWELL TECHNOLOGIES SYSTEMS
DIVISION, INC.
9210 SKY PARK COURT
SAN DIEGO, CA 92123
ATTN: K. D. PYATT, JR.

MOLZEN CORBIN & ASSOCIATES, P.A.
P. O. BOX 9144
ALBUQUERQUE, NM 87119
ATTN: TECHNICAL LIBRARY

NICHOLS RESEARCH CORPORATION
4090 SOUTH MEMORIAL PARKWAY
P. O. BOX 400002
HUNTSVILLE, AL 35815-1502
ATTN: R. BYRN
ATTN: S. R. BERRY

PACIFIC-SIERRA RESEARCH
OPERATING COMPANY OF VERID
29801 28TH STREET, 2ND FLOOR
SANTA MONICA, CA 90405
ATTN: H. BRODE

PACIFIC-SIERRA RESEARCH CORPORATION
WASHINGTON OPERATIONS
1400 KEY BOULEVARD, SUITE 700
ARLINGTON, VA 22209
ATTN: M. ALLERDING

PHYSITRON INC
3304A WESTMILL DR
HUNTSVILLE, AL 35805-6132
ATTN: M. PRICE

RAYTHEON COMPANY
ATTN: D. LEPPOLD, MS55
P. O. BOX 12248
ST PETERSBURG, FL 33733-2248
ATTN: MS 3, TECHNICAL INFORMATION
CENTER

SCIENCE APPLICATIONS INT'L CORPORATION
2111 EISENHOWER AVENUE, SUITE 303
ALEXANDRIA, VA 22314
ATTN: J. COCKAYNE, SUITE 205

SCIENCE APPLICATIONS INTL CORP
10260 CAMPUS POINT DR
SAN DIEGO, CA 92121-1578
ATTN: C. HSIAO
ATTN: DR H. WILSON
ATTN: G. EGGUM, MS C2
ATTN: G. PHILLIPS, MS C2
ATTN: J. DISHON
ATTN: L. SCOTT
ATTN: TECHNICAL REPORT SYSTEM

SCIENCE APPLICATIONS INT'L CORPORATION
2109 AIR PARK ROAD, SE
ALBUQUERQUE, NM 87106
ATTN: J. GUEST

SCIENCE APPLICATIONS INT'L CORPORATION
2111 EISENHOWER AVENUE, SUITE 205
ALEXANDRIA, VA 22314
ATTN: G. BINNINGER

SCIENCE APPLICATIONS INT'L CORPORATION
ATTN: SECURITY CONTROL OFFICE
4001 N FAIRFAX DRIVE, SUITE 800
ARLINGTON, VA 22203
ATTN: M. W. MCKAY

SCIENCE APPLICATIONS INT'L CORPORATION
HUNTSVILLE DIVISION
6725 ODYSSEY DRIVE
HUNTSVILLE, AL 35806
ATTN: DIV 411, R. WESTERFELDT

SCIENCE APPLICATIONS INTL CORP
P. O. BOX 1303
MCLEAN, VA 22102
ATTN: H. SINGER

SRI INTERNATIONAL
333 RAVENSWOOD AVENUE
MENLO PARK, CA 94025-3434
ATTN: D. CURRAN
ATTN: DR J. GRAN
ATTN: E. UTHE
ATTN: J. COLTON
ATTN: J. SIMONS
ATTN: M. SANAI

TITAN CORPORATION
TITAN RESEARCH & TECHNOLOGY DIV
9410 TOPANGO CANYON BLVD, SUITE 104
CHATSWORTH, CA 91311-5771
ATTN: A. FREDERICKSON
ATTN: LIBRARY

TRW INC.
SPACE & ELECTRONICS GROUP
ONE SPACE PARK
REDONDO BEACH, CA 90278-1078
ATTN: T.I.C., S/1930

TRW OGDEN ENGINEERING OPERATIONS
1104 COUNTRY HILLS DRIVE
OGDEN, UT 84403
ATTN: W. WAMPLER

TRW - S. I. G.
STRATEGIC SYSTEMS DIVISION
P. O. BOX 1310
SAN BERNARDINO, CA 92402-1310
ATTN: N. LIPNER

TRW SPACE & DEFENSE SECTOR SPACE &
TECH GROUP OGDEN ENG OPERATIONS
P. O. BOX 804
CLEARFIELD, UT 84015-0804
ATTN: OUT6, HL DEPT/LIBRARY
ATTN: OUT6, W. WAMPLER

W J SCHAFER ASSOCIATES, INC.
321 BILLERICA ROAD
CHELMSFORD, MA 01824
ATTN: D. YOUMANS
ATTN: W. BUITENHUYS

WASHINGTON STATE UNIVERSITY
PHYSICS DEPT
PULLMAN, WA 99164-2814
ATTN: PROF Y. GUPTA

WEIDLINGER ASSOC, INC.
4410 EL CAMINO REAL, SUITE 110
LOS ALTOS, CA 94022-1049
ATTN: H. LEVINE

WEIDLINGER ASSOCIATES, INC
P. O. BOX 15880
ARLINGTON, VA 22215
ATTN: T. DEEVY

WEIDLINGER ASSOCIATES, INC.
375 HUDSON ST, 12TH FLOOR
NEW YORK, NY 10014-3656
ATTN: I. SANDLER
ATTN: R. P. DADDAZIO

DEPARTMENT OF ENERGY

UNIVERSITY OF CALIFORNIA
LAWRENCE LIVERMORE
NATIONAL LABORATORY
P. O. BOX 808
LIVERMORE, CA 94551-9900
ATTN: L-030, A. KUHL
ATTN: L-183, S. G. PEGLOW
ATTN: L-316, J. BELL
ATTN: L-999, C. E. ROSENKILDE
ATTN: TECHNICAL LIBRARY

LOS ALAMOS NATIONAL LABORATORY
P. O. BOX 1663
LOS ALAMOS, NM 87545
ATTN: CIC-14, REPORT LIBRARY

SANDIA NATIONAL LABORATORIES
ATTN: MAIL SERVICES
P. O. BOX 5800
ALBUQUERQUE, NM 87185-0459
ATTN: R. SHAGAM, MS 0328
ATTN: TECHNICAL LIBRARY,MS 0899

DEPARTMENT OF THE AIR FORCE

AFRL/MLQ
139 BARNES DRIVE, SUITE 2
TYNDALL AFB, FL 32403-5323
ATTN: MLQC, D. VICKERS
ATTN: MLQC, DR J. PORTER
ATTN: MLQP, LIBRARY
ATTN: MLQP, S. STRICKLAND

AFRL/MN
101 W. EGLIN BOULEVARD, SUITE 326
EGLIN AFB, FL 32542-6810
ATTN: MNMW, A. WEIMORTS

AIR UNIVERSITY LIBRARY
600 CHENNAULT CIRCLE
BUILDING 1405, ROOM 160
MAXWELL AFB, AL 36112-6424
ATTN: AUL-LSE

HQ USAF/IN
1700 AIR FORCE PENTAGON
WASHINGTON, DC 20330-1700
ATTN: IN RM 4A932

DEPARTMENT OF THE ARMY

DEPARTMENT OF THE ARMY
DEPUTY CHIEF OF STAFF FOR
OPERATIONS AND PLANS
THE PENTAGON
WASHINGTON, DC 20310-0460
ATTN: DAMO-SWN

COMMANDER & CHIEF OF ENGINEERS
US ARMY CORPS OF ENGINEERS
20 MASSACHUSETTS AVENUE, NW
WASHINGTON, DC 20314-1000
ATTN: CERD-L

COMMANDER
US ARMY ENGINEERING &
SUPPORT CENTER
P. O. BOX 1600
HUNTSVILLE, AL 35807-4301
ATTN: HNDED-SY

US ARMY NATIONAL GROUND
INTELLIGENCE CENTER
220 7TH STREET, NE
CHARLOTTESVILLE, VA 22901-5396
ATTN: IAFSTC-RMT

COMMANDER
US ARMY NUCLEAR & CHEMICAL AGENCY
7150 HELLER LOOP, SUITE 101
SPRINGFIELD, VA 22150-3198
ATTN: D. BASH
ATTN: G. LONG

US ARMY RESEARCH & DEVELOPMENT CENTER
WATERWAYS EXPERIMENT STATION
3909 HALLS FERRY ROAD
VICKSBURG, MS 39180-6199
ATTN: CEWES-SE-R, D. FULLER
ATTN: SD-R WELCH
ATTN: TECHNICAL LIBRARY

US ARMY RESEARCH LAB
5232 FLEMING RD
ABERDEEN PROVING GROUND, MD 21001-5067
ATTN: AMSRL-CI-LP
TECH LIBRARY, BUILDING 4600
ATTN: D. LITTARO

US ARMY RESEARCH LABORATORIES
2800 POWDER MILL ROAD
ADELPHI, MD 20783-1197
ATTN: TECHNICAL LIBRARY